# CALPHAD Modeling Based on Gibbs Energy Functions from Zero Kevin and Improved Magnetic Model: A Case Study on the Cr-Ni System

Liangyan Hao<sup>1</sup>, Andrei Ruban<sup>2</sup>, Wei Xiong<sup>1,\*</sup>

- Department of Mechanical Engineering and Materials Science, University of Pittsburgh,
   O'Hara Street, PA 15261, USA
- 2. Department of Materials Science and Engineering, KTH Royal Institute of Technology, Brinellvägen 23, SE-100 44 Stockholm, Sweden
- \* Corresponding author: w-xiong@outlook.com or weixiong@pitt.edu

## **Abstract**

The third-generation thermodynamic database that adopts the physics-based models over a wide temperature range is being developed in an attempt to increase the predictability and reliability of the CALPHAD (Calculation of Phase Diagrams) method. As a case study, this work used the new CALPHAD models to reoptimize Cr, Ni, and the Cr-Ni system. For pure elements, the Gibbs free energy of solid phases was described by a model considering various physical contributions, and the amorphous and liquid phases were described together by the two-state model. For Cr-Ni solution phases, thermodynamic modeling of the magnetic phase diagram was supported by *ab initio* calculations. This work demonstrated the way of performing thermodynamic assessment using the third-generation Gibbs free energy functions with the improved description of magnetic properties.

**Keywords:** thermodynamic database, Einstein model, Debye temperature, lattice stability, two-state model, amorphous

## 1. Introduction

Although the CALPHAD approach is an effective computational tool for materials design, the quality of the database determines the success of the CALPHAD-based method [1–8]. Meanwhile, a reliable and unified unary database is the basis for developing high-quality multicomponent thermodynamic databases. The widely adopted CALPHAD unary database so far is the second-generation released by the SGTE (Scientific Group Thermodata Europe) in 1991 [9]. Semi-empirical polynomials, which lack sufficient physical meanings, are used to describe the heat capacity above the room temperature. Low-temperature thermodynamics below 298.15 K was not modeled considering practical applications. In the second-generation CALPHAD database, the contribution to the Gibbs free energy due to intrinsic ferromagnetism is calculated according to the IHJ (Inden-Hillert-Jarl) model [10,11]. As for the antiferromagnetism, an artificial factor (-1 for bcc structure; -3 for fcc and hcp structures) was adopted by Hertzman and Sundman [12] to scale the antiferromagnetic properties when modeling the Fe-Cr system based on an empirical factor suggested by Weiss and Tauer [13]. Recently, issues of the IHJ model and associated artifacts have been identified by Xiong et al. [14] with an improved model proposed. For the sake of convenience in discussion, we refer to it as the IHX (Inden-Hillert-Xiong) model in this work.

The CALPHAD community realized the drawbacks of the SGTE database [9]. Since the Ringberg workshop in 1995 [15], attempts have been continuously made to develop the third-generation database with improved thermodynamic models. For example, a model [16,17] that incorporates the contributions from the harmonic and anharmonic lattice vibrations, electronic excitations, and magnetism, is used to describe the heat capacity of a solid phase. The two-state model [18] is employed to model the Gibbs free energy of the liquid and amorphous phases, where they are assumed as one phase that consists of liquid-like and solid-like atoms. The IHX model, which treats the Curie and Néel temperatures separately and replaces the average with the effective magnetic moment, is applied to predict the magnetic ordering free energy. It can be expected that the adoption of these physically based models in the third-generation CALPHAD database will lead to a significantly improved thermodynamic description in an extended temperature range. Especially, the third-generation thermodynamic database with higher fidelity will accelerate materials discovery and design.

So far, most of the published works about the development of the third-generation CALPHAD database focus on pure elements [17,19–27]. Several works have also been reported for binary systems such as Fe-Cr [28], Fe-Mn [29], Al-Zn [30], and Ti-V [27]. In this

work, a case study on the Cr-Ni binary is performed to stimulate more research related to the third-generation CALPHAD modeling.

The Cr-Ni system is a critical subsystem of many industrial multicomponent alloys such as steels and superalloys. More importantly, both antiferromagnetism and ferromagnetism are possible to exhibit in Cr-Ni alloys with varying compositions. Therefore, this system is suitable for demonstrating how artifacts of magnetic phase diagrams are caused when using the IHJ model and how they are properly addressed by applying the IHX model.

In this work, the third-generation CALPHAD models will be introduced at first. Second, physical quantities critical to developing the third-generation unary database will be summarized. Third, details about the literature review, *ab initio* calculations, and thermodynamic assessment will be introduced. Finally, the new descriptions of Cr, Ni, and Cr-Ni will be presented and discussed.

## 2. The third-generation thermodynamic models

## 2.1. Solid phase

This model uses the Einstein model to describe the harmonic vibrational heat capacity. Meanwhile, it considers the contributions from electronic excitation, anharmonic lattice vibration, dilatation correction, and magnetism [17]:

$$C_p = 3R(\frac{\theta_E}{T})^2 \frac{e^{\theta_E/T}}{(e^{\theta_E/T} - 1)^2} + aT + bT^4 + C_p^{mag}$$
 (1)

where R is the gas constant,  $\theta_E$  is the Einstein temperature, and  $C_p^{mag}$  is the contribution due to the intrinsic magnetism of the element. Although the Debye model better predicts the low-temperature dependence of heat capacity ( $T^8$  law) than the Einstein model, the latter is adopted due to ease of integration. The linear term in Eq. (1) stands for the electronic heat capacity, and a is close to the electronic heat capacity coefficient. The third term accounts for the conversion between  $C_V$  (heat capacity at constant volume) and  $C_p$  (heat capacity at constant pressure) and anharmonic lattice vibration. According to Chen and Sundman's suggestion [17], only  $T^4$  term is included here. However, more terms, like  $T^2$  and  $T^3$ , may be added to fit the heat capacity data within the intermediate temperature range [19]. The Gibbs free energy of a solid phase below its melting point can be derived from Eq. (1):

$$G = E_0 + 1.5R\theta_E + 3RT \ln[1 - \exp(-\theta_E/T)] - \frac{a}{2}T^2 - \frac{b}{20}T^5 + G^{mag}$$
 (2)

where  $E_0$  is the cohesive energy at 0 K, which can be predicted by *ab initio* modeling.

As for the Gibbs free energy beyond the melting point, Chen and Sundman [31] proposed

the following expression:

$$G = 1.5R\theta_E + 3RT ln[1 - \exp(-\theta_E/T)] + H' - S'T$$

$$+ a'T(1 - lnT) - \frac{b'}{30}T^{-5} - \frac{c'}{132}T^{-11} + G^{mag}$$
(3)

where H', S', a', and b' make sure that the enthalpy, entropy, heat capacity, and the first derivative of the heat capacity, respectively, are continuous around the melting point. The  $T^{-11}$  term is added to prevent the solid phase from being stable again at very high temperatures. Recently, Sundman et al. [32] proposed another alternative to avoid discontinuous description of various thermodynamic properties, *i.e.*, the so called equal-entropy criterion. They [32] suggested a direct extrapolation of Gibbs free energy function above the melting point but the solid phases that have entropy higher than the liquid phase should be removed during equilibrium calculation. This criterion has been implemented in the OpenCalphad software [33].

## 2.2. Liquid and amorphous phases

The third-generation CALPHAD models consider the two states for the liquid phase, *i.e.*, the amorphous-like state where atoms only have the vibrational degree of freedom, and the liquid-like state where atoms also have the translational degree of freedom. At low temperatures, the amorphous-like state predominates, whereas at high temperatures, the liquid-like state predominates. The Gibbs free energy of the liquid phase is calculated by the two-state model [18,34]:

$$G = G^{am} - RT ln[1 + \exp(-\Delta G_d / RT)]$$
(4)

where  $G^{am}$  stands for the Gibbs free energy when all atoms are amorphous-like. The expression of  $G^{am}$  is similar to Eq. (2) but excludes the dilatational correction and anharmonic contribution:

$$G^{am} = 1.5R\theta_E + 3RTln\left[1 - \exp\left(-\frac{\theta_E}{T}\right)\right] + D + ET^2 + G^{mag}$$
 (5)

where  $\theta_E$  is the Einstein temperature of the amorphous phase.  $\Delta G_d$  denotes the Gibbs free energy difference between these two states and is temperature-dependent:

$$\Delta G_d = A + BT + CT lnT \tag{6}$$

B is assumed to be the negative entropy of melting [17]. C is used when the first two terms in Eq. (6) are not enough to satisfactorily fit the experimental data. Other parameters, including A, D, and E, are optimized using the melting point, the enthalpy and entropy of fusion, and the heat capacity of the liquid as well as amorphous phase if possible.

# 2.3. The IHX magnetic model

The IHX magnetic model [14] accepts the modification proposed by Chen and Sundman [17] and calculates the magnetic ordering energy by adding one more expansion term to the magnetic heat capacity expressed by the IHJ model [10,11]:

$$G^{mo} = -\frac{RT}{D}\ln(\beta + 1) \left[ 0.63570895 \left( \frac{1}{p} - 1 \right) \left( \frac{\tau^3}{6} + \frac{\tau^9}{135} + \frac{\tau^{15}}{600} + \frac{\tau^{21}}{1617} \right) \right] \qquad \tau = \frac{T}{T_{tr}} \le 1 \quad (7)$$

$$G^{mo} = -\frac{RT}{D}\ln(\beta + 1)\left(\frac{\tau^{-7}}{21} + \frac{\tau^{-21}}{630} + \frac{\tau^{-35}}{2975} + \frac{\tau^{-49}}{8232}\right) \qquad \tau = \frac{T}{T_{tr}} > 1 \quad (8)$$

where  $\beta$  is the magnetic moment per atom. p is the portion of the magnetic enthalpy caused by short-range ordering, which is structure-dependent (0.37 for a bcc phase; 0.25 for a non-bcc phase). D is a constant related to p:

$$D = 0.33471979 + 0.49649686 \left(\frac{1}{p} - 1\right) \tag{9}$$

 $T_{tr}$  is the magnetic transition temperature, which is Curie temperature  $(T_C)$  for a ferromagnetic phase and Néel temperature  $(T_N)$  for an antiferromagnetic phase.

The IHX model estimates the contribution from magnetic ordering to the Gibbs free energy of the nonmagnetic reference state. However, in Eq. (2), the  $G^{mag}$  term is added to the Gibbs free energy of the magnetic ground state. Therefore, before substituting Eqs. (7) and (8) into Eq. (2), the reference state of the magnetism needs to be converted:

$$G^{mag} = G^{pm} + G^{mo} = \left(G^{fm/afm} + G^{mdo}(\infty)\right) + G^{mo}$$

$$\tag{10}$$

where  $G^{pm}$  is the Gibbs free energy of the paramagnetic state.  $G^{fm/afm}$  represents the Gibbs free energy of the ferromagnetic or antiferromagnetic state, which is calculated by Eq. (2) excluding the last term. The magnetic ordering energy,  $G^{mo}$ , is calculated using Eqs. (7)-(8).  $G^{mdo}(\infty)$  describes the magnetic disordering energy at infinitely high temperatures:

$$G^{mdo}(\infty) = -Rln(\beta + 1)\left(T - 0.38438376\frac{T_{tr}}{pD}\right)$$
 (11)

For a magnetic solution phase, the magnetic transition temperature and magnetic moment are composition-dependent. Their compositional dependence is described by the Redlich-Kister polynomial [35]:

$$T_{tr}^{\varphi} = \sum_{i} x_{i} T_{tr,i}^{\varphi} + x_{i} x_{j} \sum_{n} {}^{n} T_{tr} (x_{i} - x_{j})^{n}$$
(12)

$$\beta^{\varphi} = \sum_{i} x_i \beta_i^{\varphi} + x_i x_j \sum_{n} {}^{n} \beta (x_i - x_j)^n$$
(13)

where  ${}^{n}T_{tr}$  and  ${}^{n}\beta$  are constants obtained by fitting experimental data.

According to the IHX model, the antiferromagnetic and ferromagnetic states should be modeled simultaneously. In order to do this, both antiferromagnetic and ferromagnetic states are assigned for a pure element. For example, if an element i is ferromagnetic with  $T_{C,i}$  experimentally or theoretically determined, a hypothetical  $T_{N,i}$  with the value of  $-T_{C,i}$  will also be defined for it. After that, both the Curie and Néel temperatures of a binary or multicomponent solution phase can be modeled separately using Eq. (12).

In addition, considering the magnetic moment difference at different atomic sites, the IHX model uses the effective magnetic moment to calculate the magnetic free energy for a solution phase. The effective magnetic moment can be calculated from the local magnetic moment:

$$\beta = \prod_{i} (\beta_i + 1)^{x_i} - 1 \tag{14}$$

where  $\beta_i$  is the magnetic moment of atom i.

# 3. Critical modeling inputs

Since the third-generation CALPHAD models are physics-based, many model parameters can be directly derived from thermochemical and thermophysical quantities. In this section, some of the critical modeling inputs are discussed to facilitate future modeling.

When modeling the Gibbs free energy using the third-generation models, critical inputs include: heat capacity, enthalpy and entropy of transition, electronic heat capacity coefficient, cohesive energy at ground state, Einstein temperature, magnetic moment, and magnetic transition temperature. The heat capacity, as well as enthalpy and entropy of transition, can be found from experimental reports, review papers about thermodynamic properties of pure elements, or handbooks compiled by Hultgren et al. [36,37], Robie and Hemingway [38], Chase [39], etc. The electronic heat capacity coefficient can be derived from the low-temperature heat capacity data. The cohesive energy at the ground state can be calculated using the *ab initio* method.

The Einstein temperature is derived from the high-temperature entropy Debye temperature  $\theta_D(0)$  through an empirical relation  $\theta_E = 0.714\theta_D(0)$  [17].  $\theta_D(0)$  can be calculated from the low-temperature limit of the Debye temperature  $\theta_D(-3)$  [31] through a ratio specific to each element. Here,  $\theta_D(n)$  are Debye temperatures derived from the *n*th moment frequency for a Debye spectrum.  $\theta_D(-3)$  can be measured by various experimental methods, including heat capacity measurement, X-ray and electron diffraction, and Mössbauer spectra. If large divergence exists among values obtained by different methods, values derived from low-temperature heat capacity measurement are preferred since here the Debye temperature will be

used to model the heat capacity.  $\theta_D(-3)$  of some elements can also be found from handbooks [40,41].  $\theta_D(-3)$  can also be obtained using *ab initio* calculations through the following expressions [42]:

$$\theta_D(-3) = \frac{h}{k} \left[ \frac{3n}{4\pi} \left( \frac{N_A \rho}{M} \right) \right]^{1/3} v_m \tag{15}$$

$$v_m = \left[\frac{1}{3} \left(\frac{2}{v_t^3} + \frac{1}{v_l^3}\right)\right]^{-1/3} \tag{16}$$

$$v_t = \left(\frac{G}{\rho}\right)^{1/2}, \ v_l = \left(\frac{3B+4G}{3\rho}\right)^{1/2}$$
 (17)

where h is Planck's constant, k is Boltzmann constant, n is the number of atoms per formula,  $N_A$  is Avogadro constant,  $\rho$  is density, and M is molecular weight.  $v_m$ ,  $v_t$ , and  $v_l$  are average, transverse, and longitudinal sound velocity, respectively. The shear modulus G and bulk modulus G can be derived from G initio calculated elastic constants. Another way to calculate G for an unstable phase is using the entropy difference relative to the standard element reference state developed in the second-generation database [30]:

$$S^{\alpha} - S^{\beta} = 3R ln \left( \frac{\theta_E^{\alpha}}{\theta_F^{\beta}} \right)$$
 (18)

where  $S^{\alpha} - S^{\beta}$  is the entropy difference between an unstable phase  $\alpha$  and a stable phase  $\beta$ , which can be taken from the SGTE database [9].  $\theta_E^{\ \alpha}$  and  $\theta_E^{\ \beta}$  are the Einstein temperatures of phase  $\alpha$  and  $\beta$ , respectively.

The magnetic moment and transition temperature can be determined through measurement of magnetization and susceptibility. Alternatively, the magnetic transition temperature can be evaluated from the anomaly in a material's properties, for example, heat capacity, thermal expansion coefficient, electric resistivity, and thermoelectric power. It can also be calculated based on the Ising model [43] and Heisenberg Hamiltonian [44], but special care should be given when using these theoretically calculated results due to relatively large uncertainty. When it comes to thermodynamic modeling of binary and higher-order systems, the third-generation database pays more attention to accurate prediction of the magnetic phase diagrams. Local magnetic moments will be obtained from experiments such as neutron diffraction or *ab initio* calculations. They are then used to calculate the effective magnetic moment via Eq. (14). It needs to be emphasized that the primary purpose of introducing the effective magnetic moment into the IHX model [14] is to represent the magnetic heat capacity. Therefore, if the effective magnetic moment derived from experiments or *ab initio* calculations fails to reproduce experimental heat capacity data, it can be adjusted accordingly [45].

## 4. Literature review

#### 4.1. Cr

## **4.1.1.** Bcc phase

The melting point of Cr is hard to measure with high precision because of its high vapor pressure near the melting point. Therefore, there is a large discrepancy between values reported in literature [36–39,46–50]. The SGTE database [9] accepted the melting point of Cr to be 2180 K, as recommended by Gurvich *et al.* [47]. However, Xiong *et al.* [51] found this value is too high when modeling the Fe-Cr phase diagram. They [51] also found similar problems exist in other Cr-based binary systems, such as Cr-Fe, Cr-C, and Cr-Hf. Therefore, they suggested to adopt a lower value, 2136 K [37,52], for the melting point of Cr. In Rudy's report [53] of transition metal phase diagrams, the melting point of Cr was measured as 2133 K with an uncertainty of ±4 K. The rationale of 2136 K was also presented by a recent experimental report from Josell *et al.* [49], which used the pulsed heating technique. To better reproduce experimental phase equilibria data in Cr-containing binary or even high-order systems during future thermodynamic assessments, the value 2136 K was adopted as the melting point for bcc Cr in this work. In the future, efforts towards determining the melting point of pure Cr with a high precision are still desired.

According to Chen and Sundman [31], the ratio of  $\theta_D(0)$  to  $\theta_D(-3)$  is 0.79 for Cr.  $\theta_D(-3)$  of bcc Cr has been derived from the low-temperature heat capacity [54–58], the intensity of X-ray and electron diffraction patterns [59–61], the center shift of the Mössbauer spectra [62], elastic constants [63,64], and vibrational entropy [65], as summarized in Table 1. It can be found that the  $\theta_D(-3)$  obtained through different methods shows a large scatter. Dubiel *et al.* [66] proposed that it is more reasonable to compare the  $\theta_D(-3)$  of a pure element measured by different researchers but with the same method since different methods rely on different mechanisms to determine the  $\theta_D(-3)$ . In this paper,  $\theta_D(-3)$  is used to fit the heat capacity data, so only values derived from the low-temperature heat capacity data should be adopted. Clusius and Franzosini [55] derived the  $\theta_D(-3)$  as 580 K via the heat capacity measurements at 10 - 273 K. According to the heat capacity reported by Heiniger [57],  $\theta_D(-3)$  is 630 K, which was accepted by several studies [58,67,68]. From considerable heat capacity data of bcc Cr at liquid helium temperatures compiled by Phillips [69], White *et al.* [58] calculated the  $\theta_D(-3)$  as 600 ± 30 K. This value is accepted in this paper, from which the  $\theta_E$  of Cr is calculated as 338 K.

From the linear term of the temperature dependence of low-temperature heat capacity data, the electronic heat capacity coefficient of bcc Cr is determined as  $1.45 \pm 0.05$  mJ/(mol·K<sup>2</sup>) by

several groups [57,58,67,69]. Therefore, it is used in this work.

The magnetic ground state of bcc Cr is complex antiferromagnetism coupled with spin density wave. A good agreement has been achieved among experimental studies about its Néel temperature according to the anomaly in heat capacity [57,70,71], neutron diffraction intensity [72,73], elastic constants [74,75], magnetic susceptibility [76], electric resistivity [71,77,78], and thermoelectric power [79]. Bacon [72] and Shull [80] reported the magnetic moment  $\beta$  of bcc Cr as 0.4 and 0.45 μ<sub>B</sub>, respectively, by integrating the intensity of all neutron diffraction peaks. Their results were questioned by Arrott and Werner [81], who analyzed the neutron intensity along different wave vectors and stated that 0.42  $\mu_B$  is only the  $\beta$  of the commensurate magnetic structure. If all possible magnetic domains are considered,  $\beta$  of bcc Cr should be 0.62 μ<sub>B</sub>. This value is consistent with that determined by Ishikawa [82] using the same method and by Evans [83] using the X-ray diffractometer equipped with the focusing optics. The magnetism of Cr has also been studied using ab initio methods [84–88]. However, the densityfunctional theory (DFT) fails to predict the spin density wave ground state for Cr [86,87], which is contradictory to the experimental results. As for DFT results about the antiferromagnetic state of Cr, it was found that the local-density approximation underestimates the equilibrium lattice constant of Cr but yields magnetic moment (0.63 µ<sub>B</sub> [85]) closer to experimental results when the experimental lattice constant is used in calculation. In contrast, the generalized gradient approximation can satisfactorily predict the equilibrium lattice constant but overestimates the magnetic moment (1.16 µ<sub>B</sub> [85]). However, both the experimental measured and theoretically calculated magnetic moments are too large to properly fit the intensity of the "λ" peak of the heat capacity curve of bcc Cr. As suggested by Andersson [89], a hypothetical value, 0.0135 μ<sub>B</sub>, should be used to fit the heat capacity data. This value, which is also called the "thermodynamic  $\beta$ ", is adopted in this work.

The heat capacity of bcc Cr below 300 K has been studied by several researchers [54,55,90,91] and the results agree well with each other. Based on the critical evaluation of these data, researchers [37–39] integrated the  $C_p$  vs. T curve to yield the  $H^o(298.15 \text{ K}) - H(0 \text{ K}) = 4850 \text{ J/mol}$  and the  $C_p/T$  vs. T curve to yield the  $S(298.15 \text{ K}) = 23.62 \text{ J/(mol \cdot K)}$ , which are adopted in this work. The heat capacity data near the Néel temperature [70,92,93] are also consistent with each other. As for the high-temperature heat capacity, a good agreement is achieved among data reported by Armstrong and Grayson-Smith [94], Krauss [95], and Kohlhaas *et al.* [96]. The heat capacity data above 1873 K in the study of Umino [97] are less reliable since the purity of the sample is low (95.39 wt.%), and the melting point of bcc Cr is

highly underestimated (1873 K). Data reported by Bendick [67] and Jaeger [98] deviate from others' data [94–96], especially above 1000 K.

## 4.1.2. Fcc phase

 $\theta_D(-3)$  of fcc Cr was derived from the theoretically calculated bulk modulus as 626 K [99]. Assuming that the ratio of  $\theta_D(0)$  to  $\theta_D(-3)$  for fcc Cr is the same as for bcc Cr [17],  $\theta_D(0)$  is 495 K, and  $\theta_E$  is 353 K for fcc Cr. Large discrepancy exists between the lattice stability of fcc Cr calculated by the *ab initio* method [100] and that evaluated in the SGTE database [9]. Since the lattice stability calculated using the *ab initio* method is valid at 0 K, whereas that determined by the CALPHAD approach comes from extrapolation of high temperature phase equilibria data, the latter is preferred during thermodynamic optimization [101]. Due to the unstable nature of fcc Cr, the reliability of the ab initio calculated energy at 0 K is uncertain. Following the suggestions of Grimvall [101], the lattice stability of unstable fcc Cr extrapolated by the CALPHAD community from binary and high-order systems is preferred during the present thermodynamic optimization.

According to the SGTE database [9], fcc Cr is antiferromagnetic with a Néel temperature of 367 K and a magnetic moment of  $0.82~\mu_B$ . Owing to a lack of experimental results and atomistic simulations, the magnetism of fcc Cr was estimated based on the extrapolation from binary systems by Chin *et al.* [102]. However, these extrapolated magnetic properties were questioned by Xiong *et al.* [14] and in fact need to be further confirmed before used in thermodynamic modeling. The spin-polarization calculation results indicated that neither ferromagnetic nor antiferromagnetic state is energetically favorable for fcc Cr [99]. *Ab initio* calculations in this study also demonstrated that fcc Cr is nonmagnetic at 0 K. Thus, the magnetic contribution is not included for fcc Cr in this work.

## 4.1.3. Liquid and amorphous phases

According to Grimvall's suggestion [103],  $\theta_D(-3)$  for the amorphous phase is 70 - 85% of that stable crystalline phase. Since there is no experimental information about  $\theta_D(-3)$  of amorphous Cr, this empirical relation is adopted, from which the  $\theta_E$  is calculated equal to 237 - 288 K. The enthalpy of liquid Cr was measured by Lin and Frohberg [48] using levitation calorimeter, from which they derived a constant value (50.71 J/(mol·K)) as the heat capacity of liquid Cr. The enthalpy and entropy of fusion for Cr were also reported in the above work [48].

#### 4.2. Ni

## **4.2.1. Fcc phase**

As presented in Table 3,  $\theta_D$ (-3) and the electronic heat capacity coefficient of fcc Ni reported

by different researchers [104–112] are in relatively good agreement with each other. All of these data were derived from the low-temperature heat capacity measurement. Desai [113] presented a comprehensive review of literature about the thermodynamic properties of Ni before 1987, from which  $\theta_D(-3)$  and the electronic heat capacity coefficient of fcc Ni were evaluated as 472 K and 7.055 mJ/(mol·K<sup>2</sup>), respectively. Taking the ratio  $\theta_D(0)/\theta_D(-3)$  for fcc Ni as 0.84 [31], the  $\theta_E$  is 283 K.

The fcc Ni is ferromagnetic. Its magnetic properties reported in the literature are listed in Table 4. From the magnetization vs. T curve, Crangle and Hallam [114] extrapolated the Curie temperature of fcc Ni as 633 K. Other measurements, including magnetic behaviors [115,116], heat capacity [112,117,118], thermoelectric properties [119], and thermal expansion [120], also suggested the Curie temperature of fcc Ni is  $633\pm7$  K. The experimental [115,116,121] and theoretically calculated [122,123] magnetic moments of fcc Ni are quite consistent (Table 4). However, none of these values (around  $0.6 \mu_B$ ) can satisfactorily fit the intensity of the " $\lambda$ " peak of the  $C_p$  curve. Therefore, the thermodynamic  $\beta$  of fcc Ni is assumed to be  $0.52 \mu_B$ , as suggested by the SGTE database [9].

The heat capacity of fcc Ni has been extensively studied [97,104,112,119,124–136] and there is a good agreement among most of the results. Desai [113] performed a comprehensive literature review about experimental results of heat capacity,  $H^{\circ}(298.15 \text{ K}) - H(0 \text{ K})$ , S(298.15 K), enthalpy of fusion, and entropy of fusion for pure Ni before 1984. These data were directly used in thermodynamic assessment of Ni by this work.

#### 4.2.2. Bcc phase

Following the assumption of Chen and Sundman [17] that the same  $\theta_E$  can be chosen for fcc and bcc Fe,  $\theta_E$  of bcc Ni is assumed to be the same as  $\theta_E$  of fcc Ni since the former is not available. The cohesive energy difference between bcc and fcc Ni, which is calculated using the *ab initio* approach, is consistent with the lattice stability recommended by the SGTE database [9].

The bcc Ni is ferromagnetic. Tian *et al.* [137] successfully synthesized the metastable bcc Ni thin films on the GaAs(001) substrate via the molecular beam epitaxy method and extrapolated the Curie temperature of bulk bcc Ni as 456 K from the Curie temperature vs. thin film thickness curve. Tian *et al.* [137] also determined the magnetic moment of bcc Ni is 0.52±0.08 μ<sub>B</sub> according to magnetization measurements, which is in good agreement with the theoretically calculated values by other researchers [123,138–140].

## 4.2.3. Liquid and amorphous phases

 $\theta_D(-3)$  for amorphous Ni was determined as 272 K [141] through the extrapolation from measured  $\theta_D(-3)$  for Ni-Zr amorphous alloys with different compositions [142]. Assuming the same ratio of  $\theta_D(0)$  to  $\theta_D(-3)$  as fcc Ni [17],  $\theta_D(0)$  of amorphous Ni is 228 K, and  $\theta_E$  is 163 K. The amorphous Ni has been synthesized through the mechanical alloying followed by chemical leaching [143] and prepared by the sonochemical process [144]. Both works demonstrated that it is paramagnetic. The experimental heat capacity data for liquid Ni is not available in the literature. Therefore, this work adopts the constant value evaluated by Desai [113].

#### 4.3. Cr-Ni

## 4.3.1. Previous thermodynamic assessments

Early thermodynamic assessments [145–148] of the Cr-Ni system only included three solution phases, i.e., liquid, bcc, and fcc. In Kaufman and Nesor's work [145], the liquid phase was modeled as a regular solution, and the magnetic contribution was incorporated into the excess Gibbs free energy term. Meanwhile, thermodynamic modeling of this work [145] was not performed on the basis of the SGTE database, which had not been established at that time. In the study of Kajihara [147], the SGTE unary database was applied to model the Cr-Ni system, and the IHJ model was employed to express the magnetic contribution. Lee [148] updated the thermodynamic descriptions of Cr-Ni when modeling Cr carbides, which were adopted in the SSOL2 and BIN databases [149]. Later, the phase CrNi<sub>2</sub>, which forms through a peritectic reaction between bcc and fcc, was suggested to be included in the Cr-Ni phase diagram. On the basis of thermodynamic parameters optimized by Lee [148], Turchi et al. [150] and Chan et al. [151] modeled CrNi<sub>2</sub> as a line compound and used the formation enthalpy calculated by the ab initio method as input. However, the predicted formation temperatures of the CrNi<sub>2</sub> phase (807) K and 820 K in the work [150] and [151], respectively) are inconsistent due to the difference in the calculated formation energy. The most recent thermodynamic assessment of the Cr-Ni system was reported by Tang and Hallstedt [152], as shown in Fig. 12. They [152] considered the latest measurements [153,154] of the enthalpy of mixing for the liquid phase and adopted the experimental enthalpy of formation [155] to optimize the CrNi<sub>2</sub> phase. The predicted peritectic temperature (611 K) is in accordance with that evaluated by Nash [156]. Meanwhile, because of the magnetic transition, a Nishizawa horn [157] appears at 257 K in Fig. 12.

## 4.3.2. Phase equilibria, thermochemical and magnetic properties

From Fig. 12, it is obvious that the Cr-Ni phase diagram is characterized by a eutectic reaction that occurs at 1618 K [158,159]. The equilibrium composition for the liquid, bcc, and fcc phases are 0.46, 0.38, and 0.50 at.% Ni, respectively [12]. The CrNi<sub>2</sub> phase with the

orthorhombic structure was reported to exhibit long-range ordering below 863 K [160,161]. Since the ordering process is first-order, Nash [156] proposed that the CrNi<sub>2</sub> phase forms from a peritectic reaction, which was accepted during thermodynamic modeling [150–152].

Thermal analyses were applied to determine the solidus and liquidus of the Cr-Ni phase diagram by two groups [158,159]. On the Cr-rich side, since the samples prepared by Jenkins *et al.* [158] suffered from contamination, data reported by Sveshinikov and Pan [159] are more reliable. On the Ni-rich side, data measured by Jenkins *et al.* [158] were given more weight during optimization because extrapolating the liquidus temperature of Ni-rich alloys reported by Sveshinikov and Pan [159] will lead to a melting point higher than 1728 K for pure Ni. The bcc solvus was investigated by X-ray diffraction (XRD) [162], adiabatic calorimeter [163], and electron microscopy [164], which show great consistency. The fcc solvus has been extensively studied using XRD [162,165–167], among which the data from Jette *et al.* [162] deviate too much from others' results. The fcc solvus reported by Pugliese and Fitterer [168] is based on the activity measurement and shows a large uncertainty. Collins [164] used the energy dispersive X-ray spectroscopy (EDX) to determine the phase composition, which is less accurate than the XRD analysis.

The variation of the ordering temperature with the composition in the vicinity of 66.7 at.% Ni was studied by XRD [166,167] and neutron diffraction [160,161]. These studies all indicated that the CrNi<sub>2</sub> phase is not stoichiometric but has a homogeneity range. Karmazin [167] found that a large degree of undercooling is required to promote the formation of CrNi<sub>2</sub> and the formation temperature is 37 K lower than the decomposition temperature. Due to the very slow formation kinetics, the phase boundaries of CrNi<sub>2</sub> reported by several experimental studies [160,161,166,167] are quite different.

The enthalpy of mixing of the liquid phase on the Ni-rich side was studied by several groups [153,154,169]. The data from Batalin *et al.* [169] showed an unreasonably large demixing tendency in the liquid phase. Both Thiedemann *et al.* [153] and Saltykov *et al.* [154] found the liquid phase is a regular solution, and the enthalpy of mixing is negative on the Ni-rich side. On the Cr-rich side, the enthalpy of mixing in the liquid phase was measured by Sudavtsova [170]. This study reported very negative values and the data on the Ni-rich side diverge from other studies [153,154]. For the enthalpy of mixing in the bcc and fcc phases, good agreement was achieved among published studies [163,171,172].

Measurements [170,173–175] of the activity of Cr in liquid Cr-Ni alloys are relatively consistent with each other. Several researchers [168,176–181] studied the activity of Cr in solid phases, but the results exhibit large scatter. The data from Grube and Flad [176] show a negative

deviation from ideality and disagree greatly with other reports [168,179]. The data reported by Panish *et al.* [177] and Kubaschewski *et al.* [178] possess a large uncertainty (1 – 10% and 9%, respectively). Pugliese and Fitterer [135] employed the two-step, half-cell technique to measure the activity of Cr, but the accuracy of this technique has been questioned by several researchers [152,179,180]. The data obtained by Pugliese and Fitterer [135] are too large, and the derived enthalpy of mixing is inconsistent with that measured by Dench [163]. Values reported by Rao and Flores-Magon [180] were calculated from the results of Vintaikin and Urushadze [135], thus large errors were introduced during this process. Measurements by Mazandarany and Pehlke [179] and by Davies and Smeltzer [181] are relatively reliable, with the reported error of 2% and 1%, respectively.

Studies about the Curie temperature [116,182–186] and the magnetic moment [116,121,182,184,185] of the fcc solution phase satisfactorily agree with each other. The compositional dependence of the Néel temperature of the bcc solution phase was measured by Fukamichi and Saito [187].

# 5. Computational Modeling

## 5.1. Ab initio calculations

Due to the lack of experimental measurements, *ab initio* calculations were applied to estimate the magnetic transition temperatures and magnetic moments. Besides, the homogeneity range of the CrNi<sub>2</sub> phase was also estimated through the *ab initio* modeling. The calculations were done by the exact muffin-tin orbital (EMTO) method [188–190] as it is implemented in the Lyngby version of the code [191,192]. The details of the *ab initio* calculations, the description of the Ising Hamiltonian and the corresponding interactions, which have been used in thermodynamic Monte Carlo simulations, can be found in Ref. [193]. To determine the compositional dependence of the Curie temperature in the fcc solution phase, we used classical Heisenberg Hamiltonian:

$$H = -\sum_{p} \sum_{i,j \in p} \sum_{\alpha,\beta = Fe,Ni} J_p^{\alpha\beta} c_i^{\alpha} c_j^{\beta} e_i e_j$$
(19)

Here,  $J_p^{\alpha\beta}$  are the magnetic exchange interactions between Cr and Ni for coordination shell p, and  $e_i$  is the direction of the spin at site i.  $c_i$  takes on value 1 or 0 depending if Ni or Cr atoms occupy site i [192]. The magnetic exchange interactions were determined in the ferromagnetic state to simplify the modeling. The magnetic exchange interactions between different Ni-Ni, Ni-Cr, and Cr-Cr pairs have been calculated using the magnetic force theorem [44] by the EMTO method [194]. The self-consistent electronic structure calculations of

random alloys have been done using coherent potential approximations [190] within local density approximations at the experimental lattice constant of  $\sim 3.522$  Å. Other details of the EMTO calculations can be found in Ref. [195]. The Heisenberg Monte Carlo simulations were performed for Ni, Ni<sub>97.5</sub>Cr<sub>2.5</sub>, Ni<sub>95</sub>Cr<sub>5</sub>, and Ni<sub>90</sub>Cr<sub>10</sub> random alloys using  $8 \times 8 \times 8$  fcc simulation box and magnetic exchange interactions up to the 4th coordination shell.

## 5.2. Thermodynamic optimization

Parameter optimization for the Gibbs free energy of different phases was performed using the PARROT module of the Thermo-Calc software [149]. For pure elements, thermodynamic parameters related to thermophysical properties, as discussed in Section 3, were first fixed and then slightly adjusted during optimization. Other parameters were optimized to fit experimental heat capacity and thermodynamic data. For the Cr-Ni system, parameters in Eqs. (12) – (13) were first optimized to fit experimental or *ab initio* calculated Curie temperature, Néel temperature, and effective magnetic moment of bcc and fcc solution phases. After that, interaction parameters were optimized to reproduce the phase equilibria and thermodynamic data. Different weights were assigned to each data point according to its uncertainty, which is evaluated during the literature review. A final run was conducted to optimize all interaction parameters together with all reliable experimental data included. Considering the homogeneity range of the CrNi<sub>2</sub> phase, a two-sublattice model (Cr, Ni)<sub>1</sub>(Cr, Ni)<sub>2</sub> was used in this work. The reciprocal relationship is assumed when modeling the end-members of CrNi<sub>2</sub>:  ${}^{o}G_{Ni:Cr}^{crNi_2} = {}^{o}G_{Cr:Ni_2}^{crNi_2} + {}^{o}G_{Ni:Ni}^{crNi_2} - {}^{o}G_{Cr:Ni_2}^{crNi_2}$ .

## 6. Results and discussion

## 6.1. Thermodynamics of Cr and Ni

Table 5 lists the updated Gibbs free energy expressions for Cr and Ni using the third-generation thermodynamic models. As shown in Fig. 1, the calculated heat capacities of bcc and liquid Cr agree satisfactorily with the experimental results and change continuously within the whole temperature range. The heat capacity of liquid Cr first decreases and then increases in the vicinity of the melting point. Similar behavior was also found for other metals [17,19,25] as a possible attribute of the two-state model [30]. From Fig. 1, it can be expected that the heat capacity of liquid Cr will exceed that of bcc Cr above 6000 K, which prevents the restabilization of the bcc phase at very high temperatures. For the sake of readability, the heat capacity of the unstable fcc structure is not presented here since it is almost the same as that of bcc Cr.

Figure 2 compares the predicted heat capacity of bcc Cr using the second- and third-generation databases. It is obvious that the second-generation database is valid above the room temperature, while the third-generation database can make reasonable prediction starting from 0 K. In addition, the present descriptions avoid the kink of the calculated heat capacity around the melting point, which will prevent the abrupt change of other thermodynamic properties. From the calculated lattice stabilities of Cr by the second-generation and third-generation databases, as shown in Fig. 3, it can be observed that the melting point of Cr is changed from 2180 K to 2136 K in this work, based on the reason mentioned in Section 4.1.1.

It can be found in Fig. 4 that the improved thermodynamic descriptions of bcc Cr reproduce reasonably the experimental heat content, except for two experimental data points, which are larger than the calculated results. These two data points from the work of Umino [97] are not reliable since the melting point of Cr was highly underestimated as 1873 K. The predicted heat content of liquid Cr was not exactly fitted to data reported by Lin *et al.*[48] because overfitting these data will make the calculated entropy considerably higher than the evaluated results [37–39]. As presented in Fig. 5(a), the calculated entropy of bcc Cr is in agreement with the evaluated values [37–39]. The predicted entropy of liquid Cr deviates slightly from the evaluated values [37–39] since more efforts were made to fit the heat content data from experiments. Figure 5(b) demonstrates that the third-generation thermodynamic models comply with the third law of thermodynamics and are valid below the room temperature.

The calculated heat capacities for different structures of Ni in this work are illustrated in Fig. 6. Due to strong ferromagnetism, there is a sharp peak in the heat capacity curve of fcc and bcc Ni. Since the fcc and bcc Ni have different Curie temperatures, their heat capacity curves separate in the vicinity of the Curie temperatures, with other parts of the curves overlapping. Above the melting point, the calculated heat capacity of liquid Ni is in accordance with the constant value suggested by Desai [113]. Similarly, the heat capacity of liquid Ni exceeds that of fcc Ni at very high temperatures. Figure 7 demonstrates again that the calculated heat capacity of fcc Ni is continuous with varying temperature and agrees well with experimental results below 300 K. From Fig. 8, it can be found that the magnetic heat capacity calculated by the IHX model fits better with experimental data than the IHJ model, owing to the refined value of p in Eqs. (7) – (8). As presented in Fig. 9, the calculated Gibbs free energy differences of liquid Ni relative to fcc Ni using the second- and third-generation CALPHAD models are similar. By contrast, the calculated lattice stability of bcc Ni with reference to fcc Ni in this work is different from that in the SGTE database since this work used the *ab initio* calculated cohesive energy at 0 K [100] as input whereas the SGTE database estimated the

lattice stability based on extrapolation from binary systems. It can be indicated by Fig. 10 and Fig. 11(a) that the updated Gibbs free energy functions of Ni can satisfactorily reproduce the experimental heat content and evaluated entropy data [36,38,39,113]. From Fig. 11(b), it is proven again that the third-generation database leads to zero entropy for different phases of Ni at 0 K.

## 6.2. Magnetic phase diagram of the Cr-Ni system

The difference between the magnetic model adopted in the second- and third-generation database is demonstrated in Fig. 13. It can be found that the calculated magnetic transition temperatures of the bcc and fcc phases by the IHX model are in better accordance with experimental results than the IHJ model. As shown in Fig. 13(b)(d), the IHX model that is adopted in the third-generation database uses two independent polynomials in the form of Eq. (12) to model the experimental Curie and Néel temperatures for the bcc and fcc phase. When calculating the magnetic ordering energy, only the positive magnetic transition temperature is used. Therefore, the lines below 0 K in Fig. 13(b)(d) are merely introduced to model the Curie and Néel temperatures over the whole composition range and to avoid artificially induced magnetism. By contrast, the IHJ model uses a single polynomial to calculate both the Curie and Néel temperatures. During the calculation of the magnetic ordering energy, the Néel temperature is converted to the Curie temperature through the Weiss factor (-1 for bcc phase, -3 for non-bcc phase). The Weiss factor for scaling will introduce artificial magnetic contribution for the Cr-rich fcc phase (Fig. 13(a)) and for the bcc phase within the intermediate composition range (Fig. 13(c)). The same problem of the IHJ model can also be manifested in the calculation of the magnetic moment, as shown in Fig. 14. The predicted magnetic moment of Cr-rich fcc and bcc phases by the IHJ model deviates greatly from the ab initio calculated results. Meanwhile, the IHJ model fails to satisfactorily reproduce the theoretically calculated magnetic moment of Ni-rich bcc phase.

Owing to the inaccurate description of magnetic properties, the IHJ model introduces unrealistic magnetic ordering energy in both fcc and bcc phases, especially at low temperatures, as shown in Fig. 15(c) and (d). By contrast, according to the IHX model, the magnetic contribution will be added to the Gibbs free energy only at compositions that exhibit magnetism, as presented in Fig. 15(a) and (b). Therefore, compared with the IHJ model, the IHX model used in the third-generation database gives a more accurate description of the magnetic phase diagram as well as magnetic ordering energy.

## 6.3. Thermodynamics of the Cr-Ni system

Based on the third-generation thermodynamic descriptions of Cr and Ni, the thermodynamic parameters of the Cr-Ni system were reoptimized, as listed in Table 7. The calculated phase diagram is presented in Fig. 16, which shows that most experimental data can be well reproduced. Some of the phase boundary data cannot be fitted due to large uncertainty. For example, the fcc liquidus determined by Svechnikov and Pan [159] is unreasonable because the extrapolated melting point of Ni is too high. In the work of Pugliese and Fitterer [168] and Collins [164], the fcc solvus was determined by experimental techniques with low accuracy. The calculated eutectic temperature is 1618 K, which agrees with the reported value in literature [158,159]. According to our calculation, the CrNi<sub>2</sub> phase forms from a peritectoid reaction at 863 K. As shown in Fig. 16(b), the calculated phase region of CrNi<sub>2</sub> is narrower than that determined from experiments or Monte Carlo simulations. Actually, due to the sluggish formation of CrNi<sub>2</sub>, its phase region is impossible to be accurately measured by experiments, and thus the phase boundaries reported by different researchers [160,161,166,167] exhibit a large scatter. On the other hand, the Monte Carlo simulations tend to overestimate the stability range of an ordered phase and can only provide the farthest possible phase boundaries [196]. Therefore, higher weights were given to the experimental enthalpy of formation of CrNi<sub>2</sub> [155] and the peritectoid temperature [156] during thermodynamic optimization.

As indicated in Fig. 17(a), the calculated enthalpy of mixing in the liquid phase agrees with those reported by Thiedemann *et al.* [153] and Saltykov *et al.* [154], whereas the results in the work of Batalin *et al.* [169] and Sudavtsova [170] are not reproduced because they are problematic as mentioned in Section 4.3.2. From Fig. 17(b), it is shown that the available datasets [163,171,172] regarding the enthalpy of mixing in the solid phases are consistent, and the calculated values can reproduce them reasonably. The calculated activity of Cr in the liquid phase can reproduce the experimental results [170,173–175], as shown in Fig. 18(a). As for the activity of Cr in solid solutions, the calculated results are close to the values measured by Mazandarany [179] (Fig. 18(b)). The data reported by Grube and Flad [176] and Rao and Flores-Magon [180] are not well reproduced due to their large uncertainty.

## 7. Conclusions

In this work, the Cr-Ni system was used as a case study to introduce the way of performing a binary assessment using the third-generation Gibbs free energy functions and to demonstrate the advantage of the third-generation over the second-generation thermodynamic modeling. Emphasis was also given to the IHX model used for describing the magnetic phase diagram. Overall, we can conclude that:

- (1) Thermodynamic properties of pure elements can be accurately described over the entire temperature range using the third-generation thermodynamic models, especially for the low temperature range below 298.15 K.
- (2) The calculated phase diagram and thermodynamic properties of the Cr-Ni binary agree well with reliable experimental results. The calculated phase boundaries of CrNi<sub>2</sub> are in accordance with the homogeneity limit estimated by atomistic modeling and experiments.
- (3) The IHX model can avoid artificial magnetism in the magnetic phase diagrams and thus reasonably predict the magnetic ordering energy. The current case study calls for more research activities towards thermodynamic modeling of magnetic phase diagrams.
- (4) In order to develop a new unary database better than the SGTE pure element database released in 1991 [9], the CALPHAD community needs to make efforts together.

## **Acknowledgments**

The authors acknowledge funding from the National Science Foundation under award DMR - 1808082, and from the University of Pittsburgh, through the Central Research Development Fund (CRDF). The authors thank Prof. Malin Selleby, Dr. Moshiour Rahaman, Dr. Ursula R. Kattner, Dr. Qing Chen, Dr. Biao Hu for valuable discussions.

## **Data Availability**

The data that support the findings of this study are available from the corresponding author upon reasonable request.

# References

- [1] F. Tancret, Computational thermodynamics and genetic algorithms to design affordable γ'-strengthened nickel-iron based superalloys, Model. Simul. Mater. Sci. Eng. 20 (2012). https://doi.org/10.1088/0965-0393/20/4/045012.
- [2] R. Schmid-Fetzer, J. Gröbner, Focused development of magnesium alloys using the Calphad approach, Adv. Eng. Mater. 3 (2001) 947–961. https://doi.org/10.1002/1527-2648(200112)3:12<947::AID-ADEM947>3.0.CO;2-P.
- [3] C. Zhang, F. Zhang, S. Chen, W. Cao, Computational thermodynamics aided highentropy alloy design, Jom. 64 (2012) 839–845. https://doi.org/10.1007/s11837-012-0365-6.
- [4] Y.H. Zhang, M. Li, L.A. Godlewski, J.W. Zindel, Q. Feng, Effective design of new

- austenitic cast steels for ultra-high temperature automotive exhaust components through combined CALPHAD and experimental approaches, Mater. Sci. Eng. A. 683 (2017) 195–206. https://doi.org/10.1016/j.msea.2016.12.023.
- [5] G.B. Olson, C.J. Kuehmann, Materials genomics: From CALPHAD to flight, Scr. Mater. 70 (2014) 25–30. https://doi.org/10.1016/j.scriptamat.2013.08.032.
- [6] W. Xiong, G.B. Olson, Integrated computational materials design for highperformance alloys, MRS Bull. 40 (2015) 1035–1044. https://doi.org/10.1557/mrs.2015.273.
- [7] R. Shi, A.A. Luo, Applications of CALPHAD modeling and databases in advanced lightweight metallic materials, Calphad. 62 (2018) 1–17. https://doi.org/10.1016/j.calphad.2018.04.009.
- [8] W. Xiong, G.B. Olson, Cybermaterials: Materials by design and accelerated insertion of materials, Npj Comput. Mater. 2 (2016) 15009. https://doi.org/10.1038/npjcompumats.2015.9.
- [9] A.T. Dinsdale, SGTE data for pure elements, Calphad. 15 (1991) 317–425.
   https://doi.org/10.1016/0364-5916(91)90030-N.
- [10] G. Inden, 1976Ind\_.pdf, in: Proc. CALPHAD V, Max-Planck Institute Eisenforsch, Dusseldorf, Germany, 1976: pp. 1–13.
- [11] M. Hillert, M. Jarl, A model for alloying in ferromagnetic metals, Calphad. 2 (1978) 227–238. https://doi.org/10.1016/0364-5916(78)90011-1.
- [12] S. Hertzman, B. Sundman, A thermodynamic analysis of the Fe-Cr system, Calphad. 6 (1982) 67–80. https://doi.org/10.1016/0364-5916(82)90018-9.
- [13] R.J. Weiss, K.J. Tauer, Theory of Alloy Phases, ASM, Cleveland, Ohio, 1956.
- [14] W. Xiong, Q. Chen, P.A. Korzhavyi, M. Selleby, An improved magnetic model for thermodynamic modeling, Calphad. 39 (2012) 11–20. https://doi.org/10.1016/j.calphad.2012.07.002.
- [15] B. Sundman, F. Aldinger, The Ringberg workshop 1995 on unary data for elements and other end-members of solutions, Calphad. 19 (1995) 433–436. https://doi.org/10.1016/0364-5916(96)00001-6.
- [16] M.W. Chase, I. Ansara, A. Dinsdale, G. Eriksson, G. Grimvall, L. Hoglund, H. Yokokawa, Group 1: heat capacity models for crystalline phases from 0 K to 6000 K, Calphad. 19 (1995) 437–447. https://doi.org/10.1016/0364-5916(96)00002-8.
- [17] Q. Chen, B. Sundman, Modeling of thermodynamic properties for bcc, fcc, liquid, and amorphous iron, J. Phase Equilibria. 22 (2001) 631–644.

- https://doi.org/10.1361/105497101770332442.
- [18] J. Ågren, B. Cheynet, M.T. Clavaguera-Mora, K. Hack, J. Hertz, F. Sommer, U. Kattner, Group 2: Extrapolation of the heat capacity in liquid and amorphous phases, Calphad. 19 (1995) 449–480. https://doi.org/10.1016/0364-5916(96)00003-X.
- [19] S. Bigdeli, H. Mao, M. Selleby, On the third-generation Calphad databases: An updated description of Mn, Phys. Status Solidi Basic Res. 252 (2015) 2199–2208. https://doi.org/10.1002/pssb.201552203.
- [20] S. Bigdeli, H. Ehtehsami, Q. Chen, H. Mao, P. Korzhavy, M. Selleby, New description of metastable hcp phase for unaries Fe and Mn: Coupling between first-principles calculations and CALPHAD modeling, Phys. Status Solidi Basic Res. 253 (2016) 1830–1836. https://doi.org/10.1002/pssb.201600096.
- [21] S. Bigdeli, L.F. Zhu, A. Glensk, B. Grabowski, B. Lindahl, T. Hickel, M. Selleby, An insight into using DFT data for Calphad modeling of solid phases in the third generation of Calphad databases, a case study for Al, Calphad. 65 (2019) 79–85. https://doi.org/10.1016/j.calphad.2019.02.008.
- [22] S. Bigdeli, Q. Chen, M. Selleby, A new description of pure C in developing the third generation of calphad databases, J. Phase Equilibria Diffus. 39 (2018) 832–840. https://doi.org/10.1007/s11669-018-0679-3.
- [23] Z. Li, S. Bigdeli, H. Mao, Q. Chen, M. Selleby, Thermodynamic evaluation of pure Co for the third generation of thermodynamic databases, Phys. Status Solidi Basic Res. 254 (2017). https://doi.org/10.1002/pssb.201600231.
- [24] A. V. Khvan, A.T. Dinsdale, I.A. Uspenskaya, M. Zhilin, T. Babkina, A.M. Phiri, A thermodynamic description of data for pure Pb from 0 K using the expanded Einstein model for the solid and the two state model for the liquid phase, Calphad. 60 (2018) 144–155. https://doi.org/10.1016/j.calphad.2017.12.008.
- [25] A. V. Khvan, I.A. Uspenskaya, N.M. Aristova, Q. Chen, G. Trimarchi, N.M. Konstantinova, A.T. Dinsdale, Description of the thermodynamic properties of pure gold in the solid and liquid states from 0 K, Calphad. 68 (2020) 101724. https://doi.org/10.1016/j.calphad.2019.101724.
- [26] A. V. Khvan, T. Babkina, A.T. Dinsdale, I.A. Uspenskaya, I. V. Fartushna, A.I. Druzhinina, A.B. Syzdykova, M.P. Belov, I.A. Abrikosov, Thermodynamic properties of tin: Part I Experimental investigation, ab-initio modelling of α-, β-phase and a thermodynamic description for pure metal in solid and liquid state from 0 K, Calphad. 65 (2019) 50–72. https://doi.org/10.1016/j.calphad.2019.02.003.

- [27] B. Hu, S. Sridar, L. Hao, W. Xiong, A new thermodynamic modeling of the Ti–V system including the metastable ω phase, Intermetallics. 122 (2020) 106791. https://doi.org/10.1016/j.intermet.2020.106791.
- [28] W. Xiong, P. Hedström, M. Selleby, J. Odqvist, M. Thuvander, Q. Chen, An improved thermodynamic modeling of the Fe-Cr system down to zero kelvin coupled with key experiments, Calphad. 35 (2011) 355–366. https://doi.org/10.1016/j.calphad.2011.05.002.
- [29] S. Bigdeli, M. Selleby, A thermodynamic assessment of the binary Fe-Mn system for the third generation of Calphad databases, Calphad. 64 (2019) 185–195. https://doi.org/10.1016/j.calphad.2018.11.011.
- [30] A. Dinsdale, O. Zobac, A. Kroupa, A. Khvan, Use of third generation data for the elements to model the thermodynamics of binary alloy systems: Part 1 The critical assessment of data for the Al-Zn system, Calphad. 68 (2020) 101723. https://doi.org/10.1016/j.calphad.2019.101723.
- [31] Q. Chen, B. Sundman, Calculation of debye temperature for crystalline structures—a case study on Ti, Zr, and Hf, Acta Mater. 49 (2001) 947–961. https://doi.org/10.1016/S1359-6454(01)00002-7.
- [32] B. Sundman, U.R. Kattner, M. Hillert, M. Selleby, J. Ågren, S. Bigdeli, Q. Chen, A. Dinsdale, B. Hallstedt, A. Khvan, H. Mao, R. Otis, A method for handling the extrapolation of solid crystalline phases to temperatures far above their melting point, Calphad. 68 (2020) 101737. https://doi.org/10.1016/j.calphad.2020.101737.
- [33] B. Sundman, U.R. Kattner, M. Palumbo, S.G. Fries, OpenCalphad a free thermodynamic software, Integr. Mater. Manuf. Innov. 4 (2015) 1–15. https://doi.org/10.1186/s40192-014-0029-1.
- [34] J. Ågren, Thermodynamics of supercooled liquids and their glass transition, Phys. Chem. Liq. 18 (1988) 123–139. https://doi.org/10.1080/00319108808078586.
- [35] O. Redlich, A.T. Kister, Algebraic representation of thermodynamic properties and the classification of solutions, Ind. Eng. Chem. 40 (1948) 345–348. https://doi.org/10.1021/ie50458a036.
- [36] R. Hultgren, Selected values of thermodynamic properties of metals and alloys, Wiley, New York, 1963.
- [37] R. Hultgren, Selected values of the thermodynamic properties of the elements, American Society for Metals, Ohio, 1973.
- [38] R.A. Robie, B.S. Hemingway, Thermodynamic properties of minerals and related

- substances at 298.15 K and 1 bar (10<sup>5</sup> pascals) pressure and at higher temperatures, U.S. G.P.O.; For sale by U.S. Geological Survey, Information Services, Washington, 1995. https://doi.org/10.3133/b2131.
- [39] M.W. Chase, NIST-JANAF thermochemical tables, 4th edition, American Chemical Society and American Institute of Physics, Washington, 1998.
- [40] C. Kittel, Introduction to solid state physics, Wiley, 2004.
- [41] W.P. Mason, Physical acoustics, Academic Press, 1965.
- [42] O.L. Anderson, A simplified method for calculating the debye temperature from elastic constants, J. Phys. Chem. Solids. 24 (1963) 909–917. https://doi.org/10.1016/0022-3697(63)90067-2.
- [43] J. Mielnicki, T. Balcerzak, V.H. Truong, G. Wiatrowski, L. Wojtczak, A simple method of basic properties description of diluted ferromagnetic alloys (Ising model, S=1/2), J. Magn. Magn. Mater. 58 (1986) 325–333. https://doi.org/10.1016/0304-8853(86)90455-5.
- [44] A.I. Liechtenstein, M.I. Katsnelson, V.. Antropov, V.A. Gubanov, Local spin density functional approach to the theory of exchange interactions in ferromagnetic metals and alloys, J. Magn. Magn. Mater. 67 (1987) 65–74. https://doi.org/10.1016/0304-8853(87)90721-9.
- [45] D. de Fontaine, S.G. Fries, G. Inden, P. Miodownik, R. Schmid-Fetzer, S.L. Chen, Workshop on thermodynamic models and data for pure elements and other endmembers of solutions: Schloβ Ringberg, Febr. 26, to March 3, 1995, Calphad. 19 (1995) 499–536. https://doi.org/10.1016/0364-5916(96)00005-3.
- [46] C.J. Smithells, S. V. Williams, Melting point of chromium, Nature. 124 (1929) 617–618. https://doi.org/10.1038/124617c0.
- [47] L. V. Gurvich, I. V. Veits, V.A. Medvedev, Calculations of Thermodynamic Properties, Nauka, Moscow, 1982.
- [48] R. Lin, M.G. Frohberg, Enthalpy measurements of solid and liquid chromium by levitation calorimetry, High Temp. High Press. 20 (1988) 539–544.
- [49] D. Josell, D. Basak, J.L. McClure, U.R. Kattner, M.E. Williams, W.J. Boettinger, M. Rappaz, Moving the pulsed heating technique beyond monolithic specimens: Experiments with coated wires, J. Mater. Res. 16 (2001) 2421–2428. https://doi.org/10.1557/JMR.2001.0332.
- [50] N.A. Dubrovinskaia, L.S. Dubrovinsky, S.K. Saxena, B. Sundman, Thermal expansion of Chromium (Cr) to melting temperature, Calphad. 21 (1997) 497–508.

- https://doi.org/10.1016/S0364-5916(98)00007-8.
- [51] W. Xiong, M. Selleby, Q. Chen, J. Odqvist, Y. Du, Phase equilibria and thermodynamic properties in the Fe-Cr system, Crit. Rev. Solid State Mater. Sci. 35 (2010) 125–152. https://doi.org/10.1080/10408431003788472.
- [52] H. Baker, H. Okamoto, ASM Handbook: Volume 3: Alloy Phase Diagrams, ASM International: Materials Park, Ohio, 1992.
- [53] E. Rudy, Ternary phase equilibria in transition metal-boron-carbon-silicon systems.
  Part V. Compendium of phase diagram data. Report AFML-TR-65-2, Dayton, Ohio, 1966.
- [54] J.A. Rayne, W.R.G. Kemp, XCIII. The heat capacities of chromium and nickel, Philos.Mag. 1 (1956) 918–925. https://doi.org/10.1080/14786435608238169.
- [55] V.K. Clusius, P. Franzosini, Ergebnisse der Tieftemperaturforschung XXXVIII Atomund Elektronenwärme des Chroms zwischen 14°K und 273°K, Zeitschrift Für Naturforsch. A. 17 (1962) 522–525. https://doi.org/10.1515/zna-1962-0611.
- [56] N. Pessall, K.P. Gupta, C.H. Cheng, P. A. Beck, Low temperature specific heat of B.C.C. alloys of 3d transition elements and aluminum, J. Phys. Chem. Solids. 25 (1964) 993–1003. https://doi.org/10.1016/0022-3697(64)90037-X.
- [57] F. Heiniger, Elektronische spezifische wärme und antiferromagnetismus in chromlegierungen, Phys. Der Kondens. Mater. 5 (1966) 285–301. https://doi.org/10.1007/BF02422668.
- [58] G.K. White, R.B. Roberts, E. Fawcett, Thermal expansion of Cr and CrV alloys. I: Experiment, J. Phys. F Met. Phys. 16 (1986) 449–459. https://doi.org/10.1088/0305-4608/16/4/009.
- [59] T. Paakkari, A determination of the Debye–Waller temperature factor and the X-ray Debye temperature for Ni, Cr, Fe, Mo and W, Acta Crystallogr. Sect. A. 30 (1974) 83–86. https://doi.org/10.1107/S0567739474000131.
- [60] L. Jithender, N. Gopikrishna, X-ray study of Debye temperatures of bcc-Fe-Cr mechanical alloys, Indian J. Phys. 87 (2013) 537–542. https://doi.org/10.1007/s12648-013-0259-7.
- [61] D. Tabor, J.M. Wilson, T.J. Bastow, Surface Debye-Waller factors for Cr(100) and Mo(100), Surf. Sci. 26 (1971) 471–489. https://doi.org/10.1016/0039-6028(71)90009-4.
- [62] S.M. Dubiel, J. Żukrowski, Debye temperature of single-crystal Cr with incommensurate and commensurate magnetic structure, EPL. 127 (2019) 10–12.

- https://doi.org/10.1209/0295-5075/127/26002.
- [63] F.H. Herbstein, Methods of measuring Debye temperatures and comparison of results for some cubic crystals, Adv. Phys. 10 (1961) 313–355. https://doi.org/10.1080/00018736100101301.
- [64] J.L. Feldman, Lattice-vibrational properties of chromium in the harmonic approximation on the basis of the tensor model, Phys. Rev. B. 1 (1970) 448–454. https://doi.org/10.1103/PhysRevB.1.448.
- [65] G. Moraitis, F. Gautier, Einstein temperature and vibrational entropy in relation to the electronic structure: I. Pure transition metals, J. Phys. F Met. Phys. 7 (1977) 1841–1851. https://doi.org/10.1088/0305-4608/7/9/026.
- [66] S.M. Dubiel, J. Cieślak, B.F.O. Costa, Debye temperature of disordered bcc-Fe-Cr alloys, J. Phys. Condens. Matter. 22 (2010) 1–6. https://doi.org/10.1088/0953-8984/22/5/055402.
- [67] W. Bendick, W. Pepperhoff, The heat capacity of Ti, V and Cr, J. Phys. F Met. Phys. 12 (1982) 1085–1090. https://doi.org/10.1088/0305-4608/12/6/009.
- [68] C. Kittel, Introduction to Solid State Physics, Wiley, New York, 1986.
- [69] N.E. Phillips, Low-temperature heat capacity of metals, Crit. Rev. Solid State Mater. Sci. 2 (1971) 467–553. https://doi.org/10.1080/10408437108243546.
- [70] R. H. Beaumont, H. Chihara, J.A. Morrison, An anomaly in the heat capacity of chromium at 38.5°C, Philos. Mag. 5 (1960) 188–191. https://doi.org/10.1080/14786436008243302.
- [71] M. B. Salamon, D. S. Simons, P. R. Garnier, Simultaneous measurement of the anomalous heat capacity and resistivity of chromium near TN, Solid State Commun. 7 (1969) 1035–1038. https://doi.org/10.1016/0038-1098(69)90464-5.
- [72] G.E. Bacon, A neutron-diffraction study of very pure chromium, Acta Crystallogr. 14 (1961) 823–829. https://doi.org/10.1107/s0365110x61002412.
- [73] S.A. Werner, A. Arrott, H. Kendrick, Temperature and magnetic-field dependence of the antiferromagnetism in pure chromium, Phys. Rev. 155 (1967) 528–539. https://doi.org/10.1103/PhysRev.155.528.
- [74] D.I. Bolef, J. De Klerk, Anomalies in the elastic constants and thermal expansion of chromium single crystals, Phys. Rev. 129 (1963) 1063–1067. https://doi.org/10.1103/PhysRev.129.1063.
- [75] L.C. Ming, M.H. Manghnani, Isothermal compression of bcc transition metals to 100 kbar, J. Appl. Phys. 49 (1978) 208–212. https://doi.org/10.1063/1.324325.

- [76] D. Bender, J. Müller, Magnetische Suszeptibilität von Chrom und Chrom-Legierungen, Phys. Der Kondens. Mater. 10 (1970) 342–366. https://doi.org/10.1007/BF02422853.
- [77] A.L. Trego, A.R. MacKintosh, Antiferromagnetism in chromium alloys. II. Transport properties, Phys. Rev. 166 (1968) 495–506. https://doi.org/10.1103/PhysRev.166.495.
- [78] B. Stebler, The resistivity anomaly in chromium near the Néel temperature, Phys. Scr. 2 (1970) 53–56. https://doi.org/10.1088/0031-8949/2/1-2/010.
- [79] A. Fote, R. Axler, H.K. Schürmann, T. Mihalisin, Thermoelectric power of chromium below the Néel temperature, Phys. Rev. B. 8 (1973) 2099–2105. https://doi.org/10.1103/PhysRevB.8.2099.
- [80] C.G. Shull, M.K. Wilkinson, Neutron diffraction studies of various transition elements, Rev. Mod. Phys. 25 (1953) 100–107. https://doi.org/10.1103/RevModPhys.25.100.
- [81] A. Arrott, S.A. Werner, H. Kendrick, Neutron-diffraction study of dilute chromium alloys with iron, Phys. Rev. 153 (1967) 624–631. https://doi.org/10.1103/PhysRev.153.624.
- [82] S.H. Yoshikazu Ishikawa, Y. Endoh, Antiferromagnetism in dilute iron chromium alloys, J. Phys. Soc. Jpn. 22 (1967) 1221–1232. https://doi.org/10.1143/JPSJ.22.1221.
- [83] P.G. Evans, E.D. Isaacs, G. Aeppli, Z. Cai, B. Lai, X-ray microdiffraction images of antiferromagnetic domain evolution in chromium, Science (80-.). 295 (2002) 1042–1045. https://doi.org/10.1126/science.1066870.
- [84] P.M. Marcus, S.L. Qiu, V.L. Moruzzi, The mechanism of antiferromagnetism in chromium, J. Phys. Condens. Matter. 10 (1998) 6541–6552. https://doi.org/10.1088/0953-8984/10/29/014.
- [85] S. Cottenier, B. De Vries, J. Meersschaut, M. Rots, What density-functional theory can tell us about the spin-density wave in Cr, J. Phys. Condens. Matter. 14 (2002) 3275–3283. https://doi.org/10.1088/0953-8984/14/12/314.
- [86] R. Hafner, D. Spišák, R. Lorenz, J. Hafner, Does density-functional theory predict a spin-density-wave ground state for Cr?, J. Phys. Condens. Matter. 13 (2001) L239–L247. https://doi.org/10.1088/0953-8984/13/11/104.
- [87] R. Hafner, D. Spišák, R. Lorenz, J. Hafner, Magnetic ground state of Cr in density-functional theory, Phys. Rev. B. 65 (2002) 1844321–1844329. https://doi.org/10.1103/PhysRevB.65.184432.
- [88] R. Soulairol, C.C. Fu, C. Barreteau, Structure and magnetism of bulk Fe and Cr: From plane waves to LCAO methods, J. Phys. Condens. Matter. 22 (2010).

- https://doi.org/10.1088/0953-8984/22/29/295502.
- [89] J.O. Andersson, Thermodynamic properties of chromium, Int. J. Thermophys. 6 (1985) 411–419. https://doi.org/10.1007/BF00500271.
- [90] C.T. Anderson, The heat capacities of chromium, chromic oxide, chromous chloride and chromic chloride at low temperatures, J. Am. Chem. Soc. 59 (1937) 488–491. https://doi.org/10.1021/ja01282a019.
- [91] G.I. Kalishevich, P.V. Geld, R.P. Krentis, The standard specific heats, entropies, and enthalpies of silicon and chromium and its alloys, Zh. Fiz. Khim. 39 (1965) 2999–3001.
- [92] T. Kemeny, B. Fogarassy, S. Arajs, C.A. Moyer, Heat-capacity studies of chromium-rich antiferromagnetic chromium-iron alloys, Phys. Rev. B. 19 (1979) 2975–2979. https://doi.org/10.1103/PhysRevB.19.2975.
- [93] I.S. Williams, E.S.R. Gopal, R. Street, The specific heat of strained and annealed chromium, J. Phys. F Met. Phys. 9 (1979) 431–445. https://doi.org/10.1088/0305-4608/9/3/007.
- [94] L.D. Armstrong, H. Grayson-Smith, High temperature calorimetry: II. Atomic heats of chromium, manganese, and cobalt between 0° and 800°C, Can. J. Res. 28a(1) (1950) 51–59. https://doi.org/10.1139/cjr50a-004.
- [95] F. Krauss, Die messung der spezifischen warme von metallen bei hohen temperaturen,Z. Met. 49 (1958) 386–392.
- [96] R. Kohlhaas, M. Braun, O. Vollmer, Die thermodynamischen funktionen des reinen eisens wärmeinhalt und spezifische wärme austenitischer eisenlegierungen und stähle, Arch. Für Das Eisenhüttenwes. 34 (1965) 391–399.
- [97] S. Umino, On the latent heat of fusion of several metals and their specific heats at high temperatures, Sci. Rep. Tôhuku Univ. 15 (1926) 597–617.
- [98] F.M. Jaeger, E. Rosenbohm, The exact measurement of the specific heats of metals at high temperatures: XVII. Calorimetrical retardation-phenomena in the case of cerium and chromium, Proc. Acad. Sci. 34 (1934) 489–497.
- [99] G. Guo, H. Wang, Calculated elastic constants and electronic and magnetic properties of bcc, fcc, and hcp Cr crystals and thin films, Phys. Rev. B Condens. Matter Mater. Phys. 62 (2000) 5136–5143. https://doi.org/10.1103/PhysRevB.62.5136.
- [100] Y. Wang, S. Curtarolo, C. Jiang, R. Arroyave, T. Wang, G. Ceder, L.Q. Chen, Z.K. Liu, Ab initio lattice stability in comparison with CALPHAD lattice stability, Calphad. 28 (2004) 79–90. https://doi.org/10.1016/j.calphad.2004.05.002.

- [101] G. Grimvall, Reconciling ab initio and semiempirical appraches to lattice stabilities, Berichte Der Bunsengesellschaft Für Phys. Chemie. 102 (1998) 1083–1087. https://doi.org/10.1002/bbpc.19981020904.
- [102] C-P. Chin, S. Hertzman, B. Sundman, An evaluation of the composition dependence of the magnetic order-disorder transition in Cr-Fe-Co-Ni alloys, 1987.
- [103] G. Grimvall, Thermophysical Properties of Materials, North Holland, 1999. https://doi.org/10.1016/B978-0-444-82794-4.X5000-1.
- [104] W.H. Keesom, C.W. Clark, The atomic heat of nickel from 1.1 to 19.0°K, Physica. 2 (1935) 513–520. https://doi.org/10.1016/S0031-8914(35)90122-7.
- [105] J.C. Walling, P.B. Bunn, The electronic specific heats of some nickel-cobalt alloys, Proc. Phys. Soc. 74 (1959) 417–423. https://doi.org/10.1088/0370-1328/74/4/305.
- [106] K.P. Gupta, C.H. Cheng, P.A. Beck, Low-temperature specific heat of F.C.C alloys of 3d-transition elements, J. Phys. Chem. Solids. 25 (1964) 73–83. https://doi.org/10.1016/0022-3697(64)90163-5.
- [107] O.L. Anderson, Determination and some uses of isotropic elastic constants of polycrystalline aggregates using single-crystal data, in: Phys. Acoust. Vol. III Part B Princ. Methods, Lattice Dyn., 1965: pp. 43–95. https://doi.org/10.1016/B978-0-12-395669-9.50009-6.
- [108] D.I. Bower, E. Claridge, I.S.T. Tsong, Low-temperature elastic constants and specific heats of F.C.C. nickel-iron alloys, Phys. Status Solidi. 29 (1968) 617–625. https://doi.org/10.1002/pssb.19680290211.
- [109] R. Ehrat, A.C. Ehrlich, D. Rivier, Low temperature specific heat of Ni and some f.c.c. Ni based alloys, J. Phys. Chem. Solids. 29 (1968) 799–806. https://doi.org/10.1016/0022-3697(68)90141-8.
- [110] R. Caudron, J.J. Meunier, P. Costa, Effect of carbon dilution on the low temperature thermal and magnetic properties of f.c.c. nickel base alloys, J. Phys. F Met. Phys. 4 (1974) 1791–1799. https://doi.org/10.1088/0305-4608/4/10/025.
- [111] I.P. Gregory, D.E. Moody, The low temperature specific heat and magnetization of binary alloys of nickel with titanium, vanadium, chromium and manganese, J. Phys. F Met. Phys. 5 (1975) 36–44. https://doi.org/10.1088/0305-4608/5/1/008.
- [112] P.J. Meschter, J.W. Wright, C.R. Brooks, T.G. Kollie, Physical contributions to the heat capacity of nickel, J. Phys. Chem. Solids. 42 (1981) 861–871. https://doi.org/10.1016/0022-3697(81)90174-8.
- [113] P.D. Desai, Thermodynamic properties of nickel, Int. J. Thermophys. 8 (1987) 763–

- 780. https://doi.org/10.1007/BF00500793.
- [114] J. Crangle, G.C. Hallam, The magnetization of face-centred cubic and body-centred cubic iron + nickel alloys, Proc. R. Soc. Lond. A. 272 (1963) 119–132. https://doi.org/10.1098/rspa.1963.0045.
- [115] J.S. Kouvel, M.E. Fisher, Detailed magnetic behavior of nickel near its curie point, Phys. Rev. 136 (1964). https://doi.org/10.1103/PhysRev.136.A1626.
- [116] H. Tange, T. Yonei, M. Goto, Forced volume magnetostriction of Ni-Cr alloys, J. Phys. Soc. Japan. 50 (1981) 454–460. https://doi.org/10.1143/JPSJ.50.454.
- [117] E.O. Schmidt, W. Leidenfrost, Adiabatic calorimeter for measurements of specific heats of powders and granular materials at 0 C to 500 C, in: Prog. Int. Res. Thermodyn. Transp. Prop., 1962: pp. 178–184. https://doi.org/10.1016/B978-1-4832-0083-5.50022-1.
- [118] M. Maszkiewicz, Specific heat of high purity nickel single crystal near the critical temperature, Phys. Status Solidi. 47 (1978) 77–80. https://doi.org/10.1002/pssa.2210470160.
- [119] A.W. Foster, XLIV. The temperature variation of the thermoelectric properties and the specific heat of nickel-chromium alloys, Philos. Mag. 18 (1934) 470–488. https://doi.org/10.1080/14786443409462519.
- [120] T.G. Kollie, Measurement of the thermal-expansion coefficient of nickel from 300 to 1000 K and determination of the power-law constants near the Curie temperature, Phys. Rev. B. 16 (1977) 4872–4881. https://doi.org/10.1103/PhysRevB.16.4872.
- [121] B. Chiffey, T.J. Hicks, The spontaneous moment of nickel-chromium alloys, Phys. Lett. A. 34A (1971) 267–268. https://doi.org/10.1016/0375-9601(71)90864-4.
- [122] T. Jarlborg, M. Peter, Electronic structure, magnetism and curie temperatures in Fe, Co and Ni, J. Magn. Magn. Mater. 42 (1984) 89–99. https://doi.org/10.1016/0304-8853(84)90293-2.
- [123] X. He, L.T. Kong, B.X. Liu, Calculation of ferromagnetic states in metastable bcc and hcp Ni by projector-augmented wave method, J. Appl. Phys. 97 (2005) 10–12. https://doi.org/10.1063/1.1903104.
- [124] R.H. Busey, W.F. Giauque, The heat capacity of nickel from 15 to 300°K. Entropy and free energy functions, J. Am. Chem. Soc. 74 (1952) 3157–3158. https://doi.org/10.1021/ja01132a058.
- [125] T.K. Engel, K.C. Jordan, G.W. Otto, D.M. Scott, High temperature differential resistance bridge calorimeter, Rev. Sci. Instrum. 35 (1964) 875–880.

- https://doi.org/10.1063/1.1746841.
- [126] M. Braun, R. Kohlhaas, Die spezifische wärme von eisen, kobalt und nickel im bereich hoher temperaturen, Phys. Status Solidi. 12 (1965) 429–444. https://doi.org/10.1002/pssb.19650120142.
- [127] R.E. Pawel, E.E. Stansbury, The specific heat of copper, nickel and copper-nickel alloys, J. Phys. Chem. Solids. 26 (1965) 607–613. https://doi.org/10.1016/0022-3697(65)90136-8.
- [128] O. Vollmer, R. Kohlhaas, M. Braun, Die schmelzwärme und die atomwärme im schmelzflüssigen bereich von eisen, kobalt und nickel, Zeitschrift Für Naturforsch. A. 21 (1966) 181–182. https://doi.org/10.1515/zna-1966-1-231.
- [129] D.L. Connelly, J.S. Loomis, D.E. Mapother, Specific heat of nickel near the curie temperature, Phys. Rev. B. 3 (1971) 924–934. https://doi.org/10.1103/PhysRevB.3.924.
- [130] A. Cezairliyan, A.P. Miiller, Heat capacity and electrical resistivity of nickel in the range 1300-1700 K measured with a pulse heating technique, Int. J. Thermophys. 4 (1983) 389–396. https://doi.org/10.1007/BF01178788.
- [131] W.H. Rodebush, J.C. Michalek, The atomic heat capacities of iron and nickel at low temperatures, J. Am. Chem. Soc. 47 (1925) 2117–2121. https://doi.org/10.1021/ja01685a006.
- [132] H. Klinkhardt, Measurement of true specific heats at high temperature by heating with thermionic electrons, Ann. Phys. 84 (1927) 167.
- [133] E. Ahrens, Über die temperaturabhängigkeit der wahren spezifischen wärme des nickels, Ann. Phys. 413 (1934) 169–181. https://doi.org/10.1002/andp.19344130204.
- [134] K.E. Grew, The specific heat of nickel and of some nickel-copper alloys, Proc. R. Soc. A Math. Phys. Eng. Sci. 145 (1934) 509–522. https://doi.org/10.1098/rspa.1934.0115.
- [135] H.L. Bronson, A.J.C. Wilson, The heat capacities of silver, nickel, zinc, cadmium and lead from -80° to 120°C, Can. J. Res. 14(a) (1936) 181–193. https://doi.org/10.1139/cjr36a-021.
- [136] C. Sykes, H. Wilkinson, The specific heat of nickel from 100°C. to 600°C., Proc. Phys. Soc. 50 (1938) 834–851. https://doi.org/10.1088/0959-5309/50/5/319.
- [137] C.S. Tian, D. Qian, D. Wu, R.H. He, Y.Z. Wu, W.X. Tang, L.F. Yin, Y.S. Shi, G.S. Dong, X.F. Jin, X.M. Jiang, F.Q. Liu, H.J. Qian, K. Sun, L.M. Wang, G. Rossi, Z.Q. Qiu, J. Shi, Body-centered-cubic Ni and its magnetic properties, Phys. Rev. Lett. 94 (2005) 1–4. https://doi.org/10.1103/PhysRevLett.94.137210.

- [138] G.Y. Guo, H.H. Wang, Gradient-corrected density functional calculation of elastic constants of Fe, Co and Ni in bcc, fcc and hcp structures, Chinese J. Phys. 38 (2000) 949–961. https://doi.org/10.1016/S0304-8853(99)00654-X.
- [139] S. Khmelevskyi, P. Mohn, Relationship between magnetic and structural properties of Ni thin films on GaAs(100) and bulk bcc Ni: First-principles calculations, Phys. Rev. B. 75 (2007) 1–4. https://doi.org/10.1103/PhysRevB.75.012411.
- [140] P. Yu, X.F. Jin, J. Kudrnovský, D.S. Wang, P. Bruno, Curie temperatures of fcc and bcc nickel and permalloy: Supercell and Green's function methods, Phys. Rev. B. 77 (2008) 1–8. https://doi.org/10.1103/PhysRevB.77.054431.
- [141] G.B. Xu, M. Meshii, P.R. Okamoto, L.E. Rehn, Crystalline-amorphous transition of NiZr2, NiZr and Ni3Zr by electron irradiation, J. Alloys Compd. 194 (1993) 401–405. https://doi.org/10.1016/0925-8388(93)90025-I.
- [142] D.G. Onn, L.Q. Wang, K. Fukamichi, Superconductivity in Fe-Zr, Ni-Zr and Cu-Zr amorphous metal alloys: Analysis of low temperature specific heat, Solid State Commun. 47 (1983) 479–483. https://doi.org/10.1016/0038-1098(83)91072-4.
- [143] S.A. Makhlouf, K. Sumiyama, E. Ivanov, H. Yamauchi, T. Hihara, K. Suzuki, Metastable b.c.c. and amorphous Ni produced by mechanical alloying and chemical leaching, Mater. Sci. Eng. A. 181 (1994) 1184–1189. https://doi.org/10.1016/0921-5093(94)90828-1.
- [144] Y. Koltypin, G. Katabi, X. Cao, R. Prozorov, A. Gedanken, Sonochemical preparation of amorphous nickel, J. Non. Cryst. Solids. 201 (1996) 159–162. https://doi.org/10.1016/0022-3093(96)00184-6.
- [145] L. Kaufman, H. Nesor, Calculation of the binary phase diagrams of iron, chromium, nickel and cobalt, Z. Met. 64 (1973) 249–257.
- [146] S. Hertzman, B. Sundman, A thermodynamic analysis of the Fe-Cr-Ni system, Scand. J. Metall. 14 (1985) 94–102.
- [147] M. Kajihara, M. Hillert, Thermodynamic evaluation of the Cr-Ni-C system, Metall. Trans. A. 21 (1990) 2777–2787. https://doi.org/10.1007/BF02646072.
- [148] B.-J. Lee, On the stability of Cr carbides, Calphad. 16 (1992) 121–149. https://doi.org/10.1016/0364-5916(92)90002-F.
- [149] B. Sundman, B. Jansson, J.O. Andersson, The Thermo-Calc databank system, Calphad. 9 (1985) 153–190. https://doi.org/10.1016/0364-5916(85)90021-5.
- [150] P.E.A. Turchi, L. Kaufman, Z.K. Liu, Modeling of Ni-Cr-Mo based alloys: Part I-phase stability, Calphad. 30 (2006) 70–87.

- https://doi.org/10.1016/j.calphad.2005.10.003.
- [151] K.S. Chan, Y.M. Pan, Y. Der Lee, Computation of Ni-Cr phase diagram via a combined first-priciples quantum mechanical and CALPHAD approach, Metall. Mater. Trans. A Phys. Metall. Mater. Sci. 37 (2006) 2039–2050. https://doi.org/10.1007/BF02586124.
- [152] F. Tang, B. Hallstedt, Using the PARROT module of Thermo-Calc with the Cr–Ni system as example, Calphad. 55 (2016) 260–269. https://doi.org/10.1016/j.calphad.2016.10.003.
- [153] U. Thiedemann, M. Rösner-kuhn, D.M. Matson, G. Kuppermann, K. Drewes, C. Merton, Mixing enthalpy measurements in the liquid ternary system iron-nickel-chromium and its binaries, Mater. Sci. 69 (1998) 3–7. https://doi.org/10.1002/srin.199801599.
- [154] P. Saltykov, V.T. Witusiewicz, I. Arpshofen, H.J. Seifert, F. Aldinger, Enthalpy of mixing of liquid Al–Cr and Cr–Ni alloys, J. Mater. Sci. Technol. 18 (2002) 167–170.
- [155] M. Hirabayashi, M. Koiwa, K. Tanaka, T. Tadaki, T. Saburi, S. Nenno, H. Nishiyama, An experimental study on the ordered alloy Ni2Cr, Trans. Japan Inst. Met. 10 (1969) 365–371. https://doi.org/10.2320/matertrans1960.10.365.
- [156] P. Nash, The Cr-Ni (Chromium-Nickel) system, Bull. Alloy Phase Diagrams. 7 (1986) 466–476. https://doi.org/10.1007/BF02867812.
- [157] T. Nishizawa, M. Hasebe, M. Ko, Thermodynamic analysis of solubility and miscibility gap in ferromagnetic alpha iron alloys, Acta Metall. 27 (1979) 817–828. https://doi.org/10.1016/0001-6160(79)90116-0.
- [158] C.H.M. Jenkins, E.H. Bucknall, C.R. Austin, G.A. Mellor, Some alloys for use at high temperatures IV: The constitution of the alloys of nickel, chromium and iron, J. Iron Steel Inst. 136 (1937) 187–220.
- [159] V.N. Svechnikov, V.M. Pan, Characteristics of the equilibrium diagram and processes of solution and precipitation in the Cr– Ni system, Sb. Nauchn. Rab. Inst. Met. Akad. Nauk. Ukr. SSR. 15 (1962) 164–178.
- [160] E.Z. Vintaikin, G.G. Urushadze, Ordering of nickel-chromium alloys, Fiz. Met. Met. 27 (1969) 895–903.
- [161] E.Z. Vintaikin, G.G. Urushadze, Neutron diffraction study of the ordering in nickel-chromium alloys, Ukr. Fiz. Zh. 15 (1970) 133–135.
- [162] E.R. Jette, V.H. Nordstrom, B. Queneau, F. Foote, X-Ray studies on the nickel-chromium system, Trans. AIME. 111 (1934) 361–373.

- [163] W.A. Dench, Adiabatic high-temperature calorimeter for the measurement of heats of alloying, Trans. Faraday Soc. 59 (1963) 1279–1292. https://doi.org/10.1039/TF9635901279.
- [164] M.J. Collins, Electron optic determination of solid phase boundaries in Ni–Cr system, Mater. Sci. Technol. 4 (1988) 560–561. https://doi.org/10.1179/mst.1988.4.6.560.
- [165] A. Taylor, R.W. Floyd, The constitution of nickel-rich alloys of the nickel-chromium-titanium system, J. Inst. Met. 80 (1951) 577–587.
- [166] H.G. Baer, Überstruktur und K-Zustand im system nickel-chrom, Z. Met. 49 (1958) 614–622.
- [167] L. Karmazin, Lattice parameter studies of structure changes of Ni-Cr Alloys in the region of Ni2Cr, Mater. Sci. Eng. 54 (1982) 247–256. https://doi.org/10.1016/0025-5416(82)90119-7.
- [168] L.A. Pugliese, G.R. Fitterer, Activities and phase boundaries in the Cr–Ni system using a solid electrolyte technique, Met. Trans. 1 (1970) 1997–2002. https://doi.org/10.1007/BF02913382.
- [169] G. Batalin, V. Kurach, V. Sudavtsova, Enthalpies of mixing of molten alloys of the nickel-chromium system, Ukr. Khim. Zh. 49 (1983) 547–548.
- [170] V.S. Sudavtsova, Thermodynamic properties of melts of Ni-Cr(Mo, W) binary systems, Russ. Met. (1999) 118–120.
- [171] O. Kubaschewski, K. Hack, Heats of formation and of transformation in the system nickel-cobalt-chromium, Z. Met. 70 (1979) 789–791.
- [172] A. Watson, F.H. Hayes, Enthalpies of formation of solid Ni-Cr and Ni-V alloys by direct reaction calorimetry, J. Alloys Compd. 220 (1995) 94–100. https://doi.org/10.1016/0925-8388(94)06008-8.
- [173] S.W. Gilby, G.R.S. Pierre, Equilibrium vapor compositions and activities of components for Fe–Cr–Ni alloys at 1600 °C, Trans. Met. Soc. AIME. 245 (1969) 1749–1758.
- [174] I. Katayama, T. Nakanishi, N. Kemori, Z. Kozuka, Thermodynamic study of liquid Ni-Cr alloys equilibrated with Cr2O3 by EMF method, Trans. Japan Inst. Met. 28 (1987) 558–563. https://doi.org/10.2320/matertrans1960.28.558.
- [175] W. Pei, O. Wijk, Activity-composition relationships in liquid nickel-chromium alloys, Scand. J. Metall. 23 (1994) 224–227.
- [176] G. Grube, M. Flad, Affinität und wärmetönung der mischkristallbildung im system chrom-nickel, Z. Elektrochem. 48 (1942) 337.

- [177] M.B. Panish, R.F. Newton, W.R. Grimes, F.F. Blankenship, Activities in the chromium-nickel system, J. Phys. Chem. 62 (1958) 980–982. https://doi.org/10.1021/j150566a023.
- [178] O. Kubaschewski, W.A. Dench, G. Heymer, The thermodynamics of the system chromium-nickel, Z. Elektrochem. 64 (1960) 801–805. https://doi.org/10.1002/bbpc.19600640605.
- [179] F.N. Mazandarany, R.D. Pehlke, Thermodynamic properties of solid alloys of chromium with nickel and iron, Metall. Trans. 4 (1973) 2067–2076. https://doi.org/10.1007/BF02643269.
- [180] M.V. Rao, E. Flores-Magon, On the thermochemistry of solid nickel-chromium alloys, Metall. Trans. 4 (1973) 2471–2473. https://doi.org/10.1007/BF02669393.
- [181] H. Davies, W.W. Smeltzer, Oxygen and metal activities of the chromium-nickel-oxygen system between 900° and 1100°C, J. Electrochem. Soc. 121 (1974) 543–549. https://doi.org/10.1149/1.2401857.
- [182] C. Sadron, Ferromagnetic moments of elements and the periodic system, Ann. Phys. 17 (1932) 371-452.
- [183] V. Marian, Curie points of ferromagnetism and absolute saturation of some alloys of nickel, Ann. Phys. 7 (1937) 459-527.
- [184] H.C. Van Elst, B. Lubach, G.J. Van den Berg, The magnetization of some nickel alloys in magnetic fields up to 15 kOe between 0°K and 300°K, Physica. 28 (1962) 1297–1317. https://doi.org/10.1016/0031-8914(62)90139-8.
- [185] M.J. Besnus, Y. Gottehrer, G. Munschy, Magnetic properties of Ni-Cr alloys, Phys. Status Solidi. 49 (1972) 597–607. https://doi.org/10.1002/pssb.2220490222.
- [186] M.A. Simpson, T.F. Smith, Thermodynamic studies and magnetic ordering of Ni-Cr alloys close to the critical composition, Aust. J. Phys. 35 (1982) 307–320. https://doi.org/10.1071/PH820307.
- [187] K. Fukamichi, H. Saito, Cr-based magnetically insensitive Invar-type alloys, Sci. Rep. Res. Tohoku A. 26 (1976) 299–332.
- [188] L. Vitos, H.L. Skriver, B. Johansson, J. Kollár, Application of the exact muffin-tin orbitals theory: The spherical cell approximation, Comput. Mater. Sci. 18 (2000) 24– 38. https://doi.org/10.1016/s0927-0256(99)00098-1.
- [189] L. Vitos, Total-energy method based on the exact muffin-tin orbitals theory, Phys. Rev. B. 64 (2001) 1–11. https://doi.org/10.1103/PhysRevB.64.014107.
- [190] L. Vitos, I.A. Abrikosov, B. Johansson, Anisotropic lattice distortions in random

- alloys from first-principles theory, Phys. Rev. Lett. 87 (2001) 156401-156401-4. https://doi.org/10.1103/PhysRevLett.87.156401.
- [191] A. V. Ruban, First-principles modeling of the Invar effect in Fe65Ni35 by the spin-wave method, Phys. Rev. B. 95 (2017) 1–13. https://doi.org/10.1103/PhysRevB.95.174432.
- [192] A. V. Ruban, V.I. Razumovskiy, First-principles based thermodynamic model of phase equilibria in bcc Fe-Cr alloys, Phys. Rev. B. 86 (2012) 1–16. https://doi.org/10.1103/PhysRevB.86.174111.
- [193] M. Rahaman, B. Johansson, A. V. Ruban, First-principles study of atomic ordering in fcc Ni-Cr alloys, Phys. Rev. B. 89 (2014) 1–12. https://doi.org/10.1103/PhysRevB.89.064103.
- [194] A. V. Ruban, M. Dehghani, Atomic configuration and properties of austenitic steels at finite temperature: Effect of longitudinal spin fluctuations, Phys. Rev. B. 94 (2016) 1–10. https://doi.org/10.1103/PhysRevB.94.104111.
- [195] M. Rahaman, B. Johansson, A. V. Ruban, First-principles study of atomic ordering in fcc Ni-Cr alloys, Phys. Rev. B - Condens. Matter Mater. Phys. 89 (2014) 1–12. https://doi.org/10.1103/PhysRevB.89.064103.
- [196] C. Wolverton, A. Zunger, Ni-Au: A testing ground for theories of phase stability,
   Comput. Mater. Sci. 8 (1997) 107–121. https://doi.org/10.1016/s0927-0256(97)00023 2.
- [197] C.F. Lucks, H.W. Deem, Thermal conductivities, heat capacities, and linear thermal expansion of five materials, Ohio, 1956.
- [198] J.B. Conway, R.A. Hein, Advances in thermophysical properties at extreme temperatures and pressure, in: 3rd Symp. Thermophys. Prop., 1965: p. 131.
- [199] M. Shiga, G.P. Pells, The optical properties of nickel above and below the Curie temperature, J. Phys. C Solid State Phys. 2 (1969) 1847–1856. https://doi.org/10.1088/0022-3719/2/10/319.

# Figure captions

- **Figure 1.** Comparison of the calculated heat capacities of bcc and liquid Cr in this work with experimental datapoints [48,54,55,67,70,90–98] and evaluation by handbooks [37,39].
- **Figure 2.** Comparison between the calculated heat capacity of bcc Cr by this work and the SGTE database [9] with experimental results [54,55,67,70,90-98]. The low-temperature heat capacity at 0 300 K is magnified in the inset.
- **Figure 3.** Comparison between the calculated Gibbs free energy differences of liquid and fcc Cr relative to bcc Cr in this work and by the SGTE database [9].
- **Figure 4.** Comparison of heat content for bcc and liquid Cr between calculation in this work and experiments [48,97,98,197,198].
- **Figure 5.** (a) Comparison between the calculated and evaluated [37–39] entropy for bcc and liquid Cr; (b) Comparison between the calculated low-temperature entropy for bcc and liquid Cr by this work and the SGTE database [9].
- **Figure 6.** Comparison of the calculated heat capacities for fcc, liquid, and bcc Ni in this work with experimental datapoints [97,104,112,119,124–136] and evaluation by handbooks [36,39,113].
- **Figure 7.** Comparison between the calculated heat capacity of fcc Ni in this work and by the SGTE database [9] with experimental results [97,104,112,119,124–136]. The low-temperature heat capacity from 0 to 300 K is magnified in the inset.
- **Figure 8.** Comparison between the calculated magnetic heat capacity for fcc Ni using the IHX and IHJ models [9]. Datapoints are derived from experiments by Chen and Sundman [17].
- **Figure 9.** Comparison between the calculated Gibbs free energy differences of liquid and bcc Ni relative to fcc Nir in this work and by the SGTE database [9].
- **Figure 10.** Comparison between the calculated and evaluated [36,38,39,113] heat content for fcc and liquid Ni.
- **Figure 11.** (a) Comparison between the calculated and evaluated [36,38,39,113] entropy for fcc and liquid Ni; (b) Comparison between the calculated low-temperature entropy for fcc and liquid Ni by this work and the SGTE database [9].
- **Figure 12.** The calculated Cr-Ni phase diagram by Tang and Hallstedt [152].
- **Figure 13.** (a) Comparisons of the calculated magnetic transition temperature by the IHX and IHJ [148] models with experimental results [116,182–186] for the fcc Cr-Ni phase; (b) Demonstration of numerical treatment using both IHJ and IHX models for Curie and Néel temperatures of the fcc alloys; (c) Comparisons of the calculated magnetic transition

temperature by the IHX and IHJ [148] models with experimental results [187] for the bcc Cr-Ni phase; (d) Demonstration of numerical treatment using both IHJ and IHX models for Curie and Néel temperatures of the bcc alloys.

**Figure 14.** Comparisons between the calculated magnetic moment in this work using the IHX model and by Lee [148] using the IHJ model for (a) the fcc; and (b) the bcc solution phases. Experimental magnetic moment data for the fcc phase are taken from [116,121,182,184,185].

**Figure 15.** Comparisons between the calculated magnetic ordering energy in this work using the IHX model and by Lee [148] using the IHJ model for (a)(b) the fcc phase; (c)(d) the bcc phase at 0, 500, and 1000 K.

**Figure 16.** (a) Comparison between the calculated and experimental [158–168] Cr-Ni phase diagram; (b) Magnification of the CrNi<sub>2</sub> phase region.

**Figure 17.** (a) Comparison between the calculated and experimental [153,154,169,170] enthalpy of mixing for the liquid phase at 1990 K. The reference state is liquid Cr and liquid Ni. (b) Comparison between the calculated and experimental [163,171,172] enthalpy of formation for the solid phases at 1538 K. The reference state is bcc Cr and fcc Ni.

**Figure 18.** (a) Comparison between the calculated and experimental [170,173–175] activity of Cr at 1873 K, relative to liquid Cr; (b) Comparison between the calculated and experimental [168,176,179,180] activity of Cr at 1273 K, relative to bcc Cr.

$\theta_{\rm D}(-3),{\rm K}$	Method	Temperature, K	Refs.
630	Heat capacity measurement	< 4.2	[54]
453	Calculation from Young's modulus	298	[63]
580	Heat capacity measurement	14-22	[55]
606	Heat capacity measurement	0-22	[56]
630	Heat capacity measurement	< 5	[57]
570	Calculation from elastic constant	298	[64]
429	Electron diffraction	298	[61]
498±6	X-ray diffraction	77-296	[59]
529	Calculation from vibrational entropy	1400	[65]
$600 \pm 30$	Heat capacity measurement	> 4.2	[58]
550±23	X-ray diffraction 298		[60]
477±55	Mössbauer spectroscopy		[62]

Table 2. Experimental investigations of the heat capacity of Cr.

_	Temperature range, K	Purity, wt.%	Experimental technique	Refs.
_	1641 – 2395	99.5	Levitation calorimeter	[48]
	1.8 - 4.2	99.8	Mechanical heat switch calorimeter	[54]
	10 - 273.2	99.9	_	[55]
	325 - 1676	99.996	Adiabatic calorimeter	[67]
	268 - 324	99.998	Adiabatic calorimeter	[70]
	56.1 - 291.1	99.35	Vacuum calorimeter	[90]
	60 - 300	99.98	_	[91]
	262 - 345	99.995	Differential scanning calorimeter	[92]
	205 - 380	99.96	Adiabatic calorimeter	[93]
	373 – 1913	95.39	Drop calorimeter	[97]
	673 - 1339	_	Drop calorimeter	[98]
	273 - 1073	99.9	Adiabatic calorimeter	[94]
	964 - 1598	99.8	Adiabatic calorimeter	[95]
	320 - 1800	_	Adiabatic calorimeter	[96]

Table 3. Comparison between the experimental and optimized Einstein temperature  $\theta_E$  and electronic heat capacity coefficient  $\gamma$  for fcc Ni. All  $\theta_D$ (-3) is derived from the heat capacity measurements.

$\theta_{\rm D}(-3)$ , K	$\theta_{\mathrm{D}}(0)^{\mathrm{a}},\mathrm{K}$	$\theta_{\rm E}{}^{\rm b},{ m K}$	$\gamma$ , mJ/(mol*K <sup>2</sup> )	Refs.
413	347	248	7.297	[104]
348±15	292	209	$6.70 \pm 0.05$	[105]
334	281	200	$7.20 \pm 0.01$	[106]
476	400	285	_	[107]
472	396	283	$7.053 \pm 0.031$	[108]
462±19	388	277	$7.12 \pm 0.02$	[109]
_	_	_	7.02	[110]
444	373	266	$7.034 \pm 0.003$	[111]
476	400	285	7.017	[112]
480	403	288	7.151	This work

 $<sup>\</sup>frac{1}{a} \theta_D(0) = 0.84 \theta_D(-3) [31]$ 

<sup>&</sup>lt;sup>b</sup>  $\theta_{\rm E} = 0.714 \theta_{\rm D}(0) [103]$ 

Table 4. The reported Curie temperature  $T_{\rm C}$  and magnetic moment  $oldsymbol{eta}$  of fcc Ni.

Properties	Value	Method	Refs.
	633	Heat capacity measurement	[112]
	633	Magnetization measurement	[114]
	627.2	Susceptibility measurement	[115]
	631	Magnetization measurement	[116]
T V	628.5	Heat capacity measurement	[117]
$T_{\rm C}$ , K	625.25	Heat capacity measurement	[118]
	626	Thermoelectric measurement	[119]
	628.5	Thermal expansion measurement	[120]
	632	Optical absorption spectrum measurement	[199]
	686	Renormalized random-phase approximation	[140]
	0.606	Magnetization measurement	[115]
	0.62	Magnetization measurement	[116]
$eta, \mu_{ m B}$	0.62	Magnetization measurement	[121]
	0.60	Linear Muffin-Tin Orbital band method	[122]
	0.60	Projector-augmented wave method	[123]

Table 5. The relationship between parameters of the third-generation CALPHAD models and physical/thermodynamic properties of a pure element.

Properties	Unit	Related parameters
Low-temperature limit of the Debye temperature, $\theta_D(-3)$	K	$ heta_{ m E}$
Electronic heat capacity coefficient, $\gamma$	$J/(mol*K^2)$	a  (Eqs. (1)  - (2))
Curie/Néel temperature, $T_{\rm C}/T_{\rm N}$	K	$T_{\rm C}/T_{\rm N}$ (Eqs. (8) – (11))
Magnetic moment, $\beta$	$\mu_{\mathrm{B}}$	$\beta$ (Eqs. (8) – (11))
$H^{\circ}(298.15 \text{ K}) - H(0 \text{ K})$	J/mol	$E_0$ (Eq. 2)
S(298.15 K)	J/(mol*K)	_
Heat capacity, $C_p$	J/(mol*K)	_
Melting point, $T_{\rm m}$	K	-
Enthalpy of fusion, $\Delta H_{\rm m}$	J/mol	H' (Eq. 3), A (Eq. 6)
Entropy of fusion, $\Delta S_{\rm m}$	J/(mol*K)	S' (Eq. 3), B (Eq. 6)

Table 6. The third-generation Gibbs free energy functions for different structures of Cr and Ni.

```
Cr:
Bcc
      T_N = 311.5, \ \beta = 0.0135, \ p = 0.37
      -8.38046986E + 03 - 7.28682048E - 04 * T^2 - 1.06068156E - 06 * T^3 + GEIN(344) +
      GMDO(\infty) + GMO
                                                                                                                                                                                                                                                                                                                                                         0 < T < 2136
       -6.62308650E + 04 + 2.72730977E + 02 * T + 3.78124734E + 01 * T - 3.7812474E + 01 * T - 3.7812474E + 01 * T - 3.7812474E + 01 * T - 3.78124744E + 01 * T - 3.7812474E + 01 * T - 3.7812474E + 01 * T - 3.781
      T * LN(T) - 2.52807159E + 17 * T^{-5} + 3.92481496E + 38 * T^{-11} + GEIN(344) +
      GMDO(\infty) + GMO
                                                                                                                                                                                                                                                                                                                                         2136 < T < 6000
Fcc
       -2.81013100E + 03 - 7.28682048E - 04 * T^2 - 1.06068156E - 06 * T^3 + GEIN(356)
       -6.06608960E + 04 + 2.72732303E + 02 * T + 3.78126465E + 01 * T - 3.78126465E + 01 *
       T * LN(T) - 2.52807159E + 17 * T^{-5} + 3.92481496E + 38 * T^{-11} + GEIN(356)
                                                                                                                                                                                                                                                                                                                                           2136 < T < 6000
Liquid and amorphous
       1.53043907E + 04 - 3.05280790E - 03 * T^2 + GEIN(260) + G2ST(4.09741845E + 04 - 1.058043907E)
       13.89 * T - 1.90447362E - 01 * T * LN(T)
                                                                                                                                                                                                                                                                                                                                                         0 < T < 6000
Ni:
Fcc
      T_C = 633, \ \beta = 0.52, \ p = 0.25
      -8.38106180E + 03 - 3.57550000E - 03 * T^2 - 6.74033504E - 15 * T^5 + GEIN(288) +
      GMDO(\infty) + GMO
                                                                                                                                                                                                                                                                                                                                                         0 < T < 2136
       -2.96324682E + 04 + 1.19928191E + 02 * T + 1.76705304E + 01 * T - 1.76705304E + 01 *
      T * LN(T) + 5.47045839E + 18 * T^{-5} - 1.10045747E + 37 * T^{-11} + GEIN(288) + 18 * T^{-10} 
      GMDO(\infty) + GMO
                                                                                                                                                                                                                                                                                                                                         2136 < T < 6000
 Bcc
      T_C = 456, \ \beta = 0.52, \ p = 0.37
       GMDO(\infty) + GMO
                                                                                                                                                                                                                                                                                                                                                         0 < T < 2136
       -2.04891168E + 04 + 1.19956846E + 02 * T + 1.76743753E + 01 * T - 1.76743753E + 01 *
      T * LN(T) + 5.47045839E + 18 * T^{-5} - 1.10045747E + 37 * T^{-11} + GEIN(288) + 1.10045747E + 3.10045747E + 3.1004747E + 3.100
      GMDO(\infty) + GMO
                                                                                                                                                                                                                                                                                                                                         2136 < T < 6000
 Liquid and amorphous
10.11E + 00 * T - 4.38342374E - 01 * T * LN(T)
                                                                                                                                                                                                                                                                                                                                                           0 < T < 6000
```

## **Auxiliary functions:**

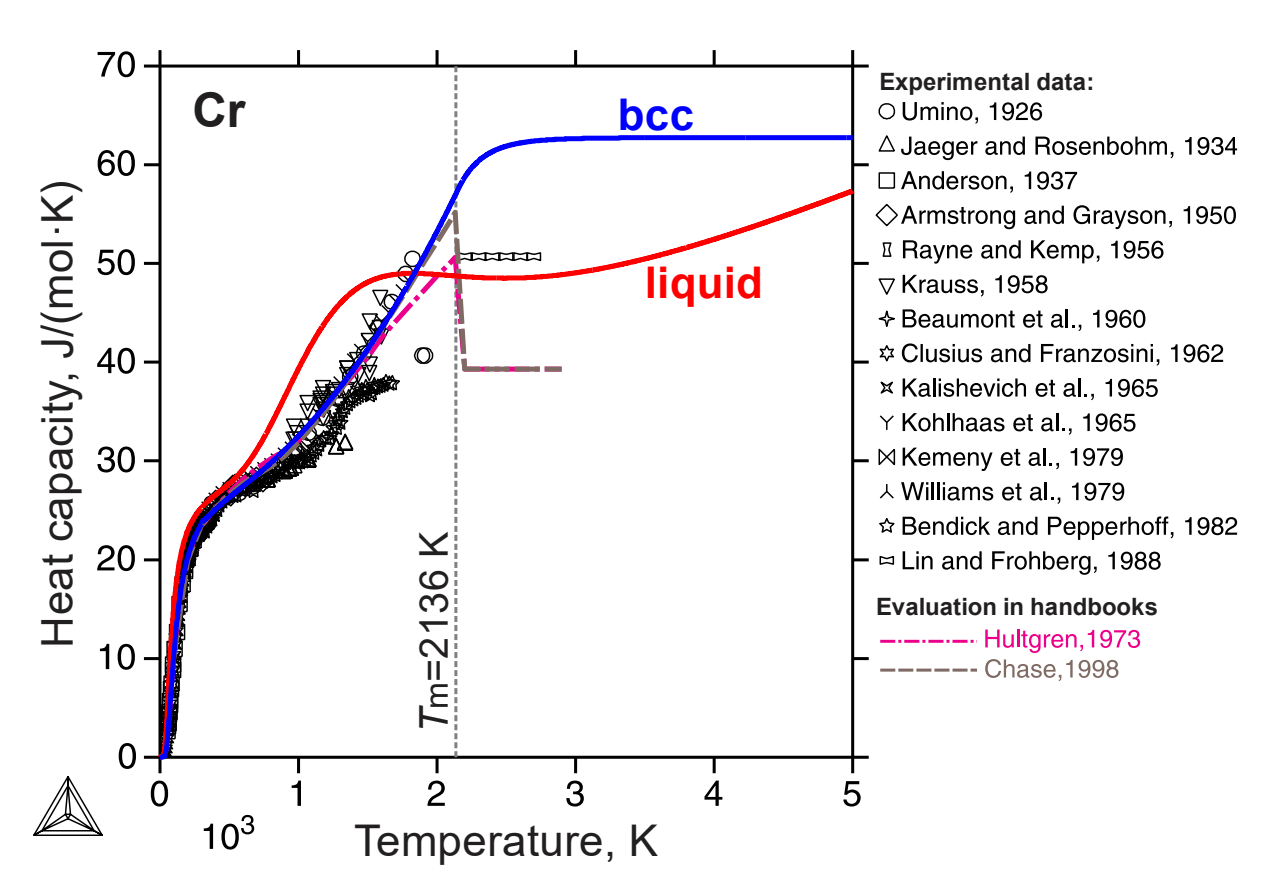
$$GEIN(\theta) = 1.5 * R * \theta + 3 * R * T * LN[1 - EXP(-\theta/T)]$$
  

$$G2ST(\Delta G_d) = -R * T * LN[1 + EXP(-\Delta G_d/(RT))]$$

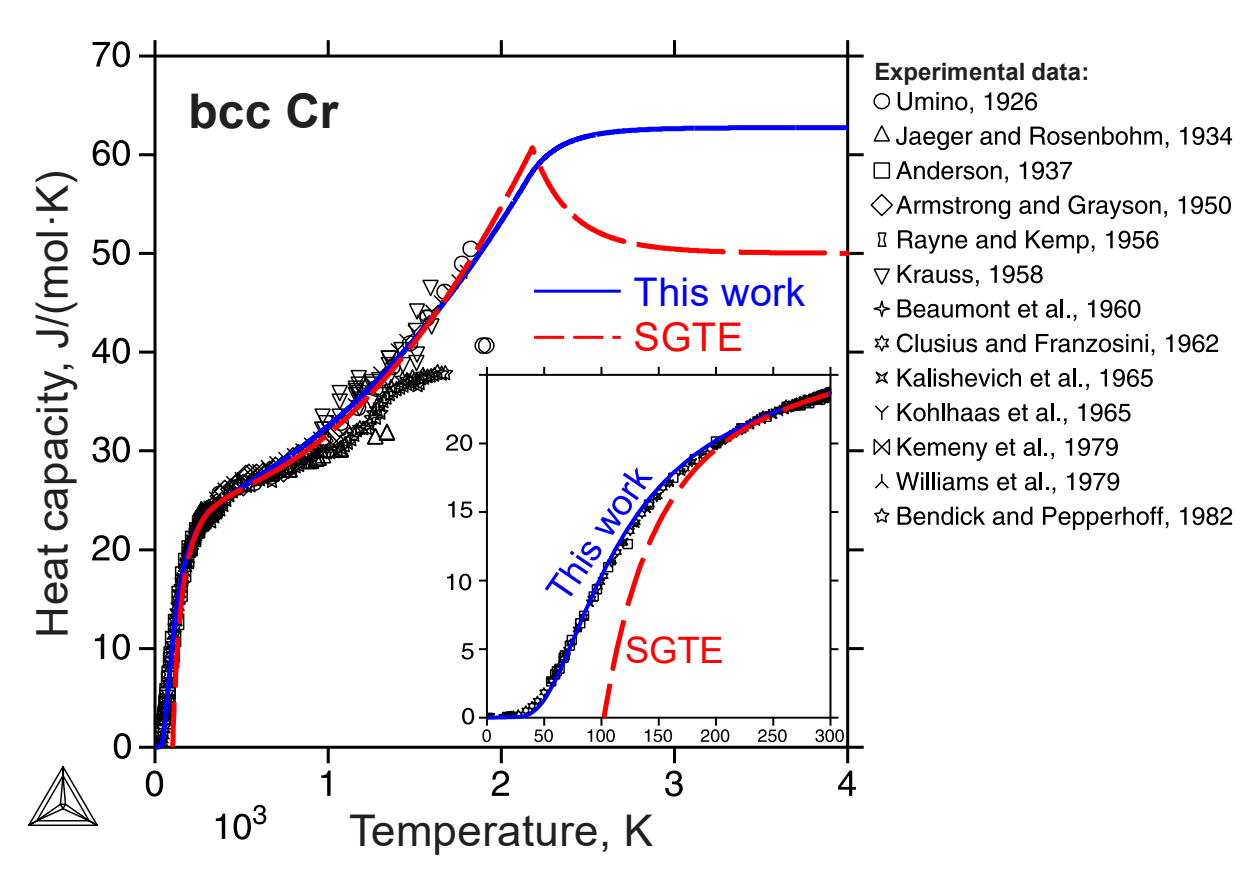
Note: All quantities are with SI units.  $GMDO(\infty)$  and GMO are calculated by Eq. (11) and Eqs. (7) – (8), respectively.

Table 7. Optimized thermodynamic parameters of each phase in the Cr-Ni system based on the third-generation lattice stabilities for Cr and Ni.

Phase	Model	Thermodynamic parameters (J/mol·atom)
Liquid	(Cr, Ni)	$^{0}L_{Cr,Ni}^{Liquid} = -14405 + 3.035 * T$
		$^{1}L_{Cr,Ni}^{Liquid}=1143$
Bcc	$(Cr, Ni)_1(Va)_3$	$^{0}L_{Cr,Ni:Va}^{Bcc} = 11748 - 12.38 * T$
		$^{1}L_{Cr,Ni:Va}^{Bcc} = 40661 - 13.099 * T$
		${}^{0}T_{CCr,Ni:Va}^{Bcc} = -11127.98$
		${}^{0}T_{N}{}^{Bcc}_{Cr,Ni:Va} = -10967.41$
		${}^0\beta^{Bcc}_{Cr,Ni:Va} = -12.24$
Fcc	$(Cr, Ni)_1(Va)_1$	${}^{0}L_{Cr,Ni:Va}^{Fcc} = 8419 - 9.413 * T$
		$^{1}L_{Cr,Ni:Va}^{Fcc} = 25557 - 12.933 * T$
		${}^{0}T_{CCr,Ni:Va}^{Fcc} = -5210.09$
		$^{0}\beta_{Cr,Ni}^{Fcc}=-4.28$
CrNi <sub>2</sub>	$(Cr, Ni)_1(Cr, Ni)_2$	${}^{o}G_{Cr:Cr}^{CrNi2} = 21081 + 3 * {}^{o}G_{Cr}^{bcc}$
		${}^{o}G_{Ni:Ni}^{CrNi2} = 88105 + 3 * {}^{o}G_{Ni}^{fcc}$
		${}^{o}G_{Cr:Ni}^{CrNi2} = -14849 + 6.277 * T + {}^{o}G_{Cr}^{bcc} + 2 * {}^{o}G_{Ni}^{fcc}$
		${}^{o}G_{Ni:Cr}^{crNi2} = 124035 - 6.277 * T + {}^{o}G_{Ni}^{fcc} + 2 * {}^{o}G_{Cr}^{bcc}$
		$^{0}L_{*:Cr,Ni}^{CrNi2} = 31662$
		$^{0}L_{Cr,Ni:*}^{CrNi2} = -88982$



**Figure 1.** Comparison of the calculated heat capacities of bcc and liquid Cr in this work with experimental datapoints [48,54,55,67,70,90–98] and evaluation by handbooks [37,39].



**Figure 2.** Comparison between the calculated heat capacity of bcc Cr by this work and the SGTE database [9] with experimental results [54,55,67,70,90-98]. The low-temperature heat capacity at 0-300 K is magnified in the inset.

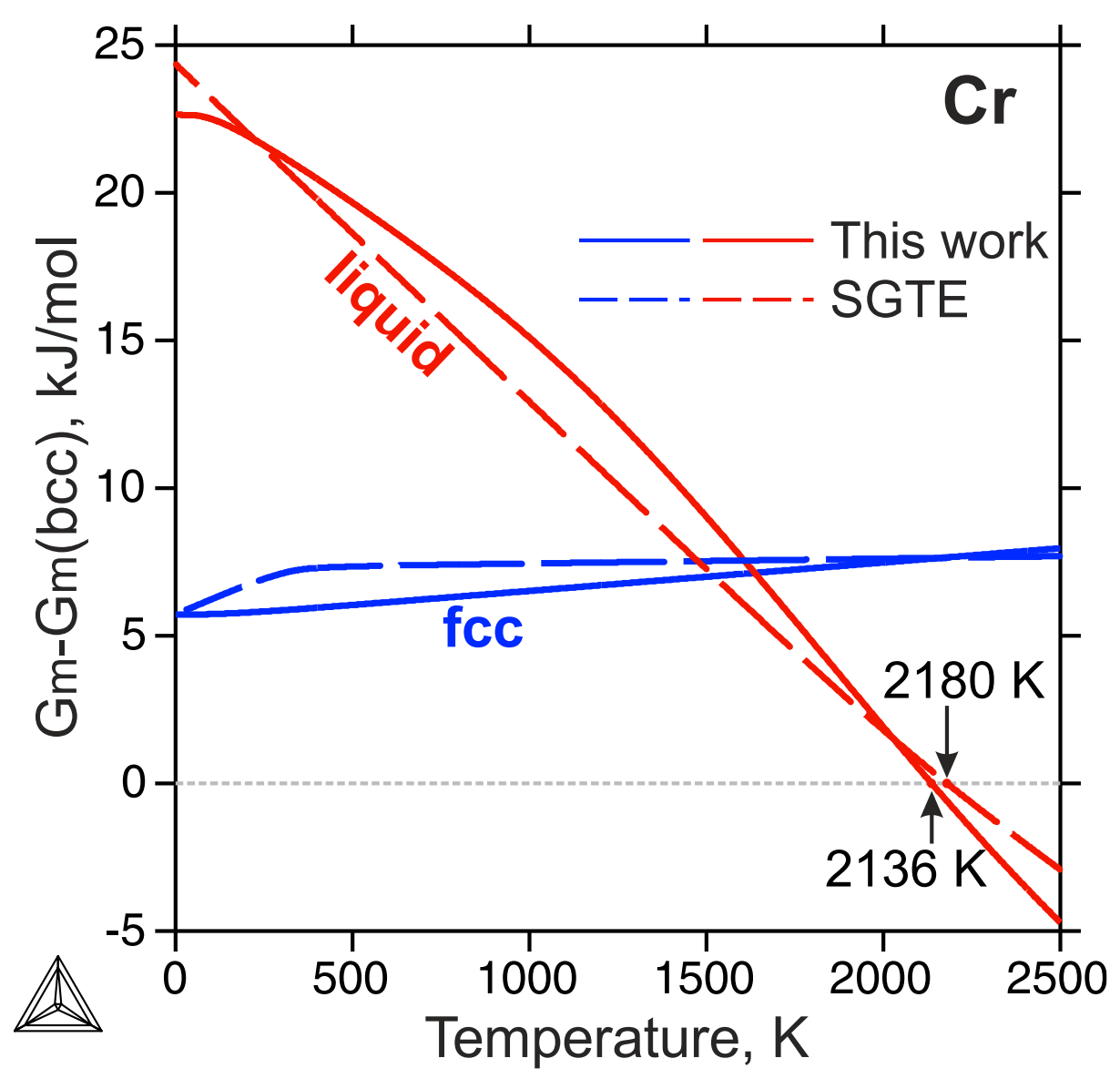


**Figure 3.** Comparison between the calculated Gibbs free energy differences of liquid and fcc Cr relative to bcc Cr in this work and by the SGTE database [9].

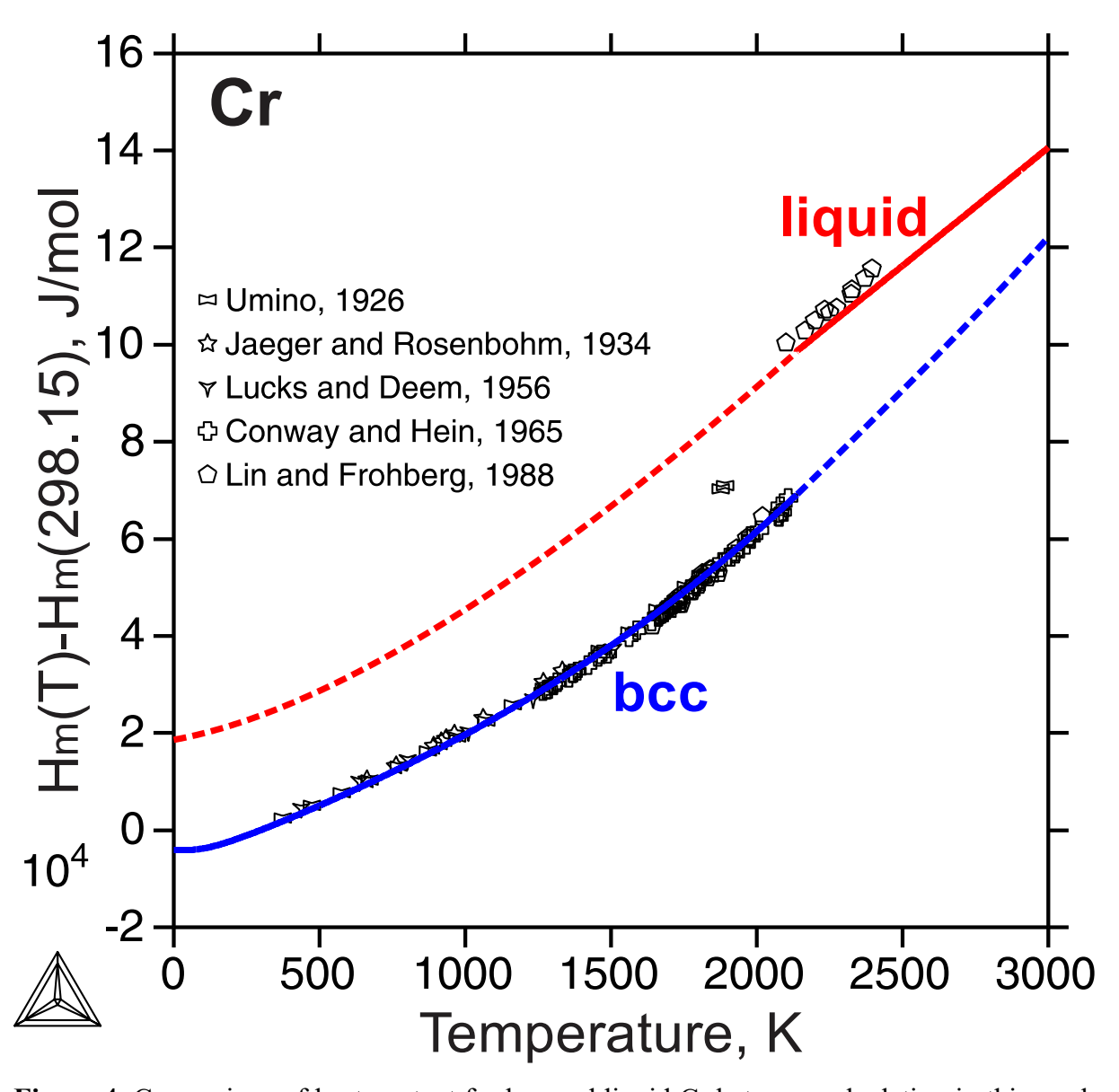


**Figure 4.** Comparison of heat content for bcc and liquid Cr between calculation in this work and experiments [48,97,98,197,198].

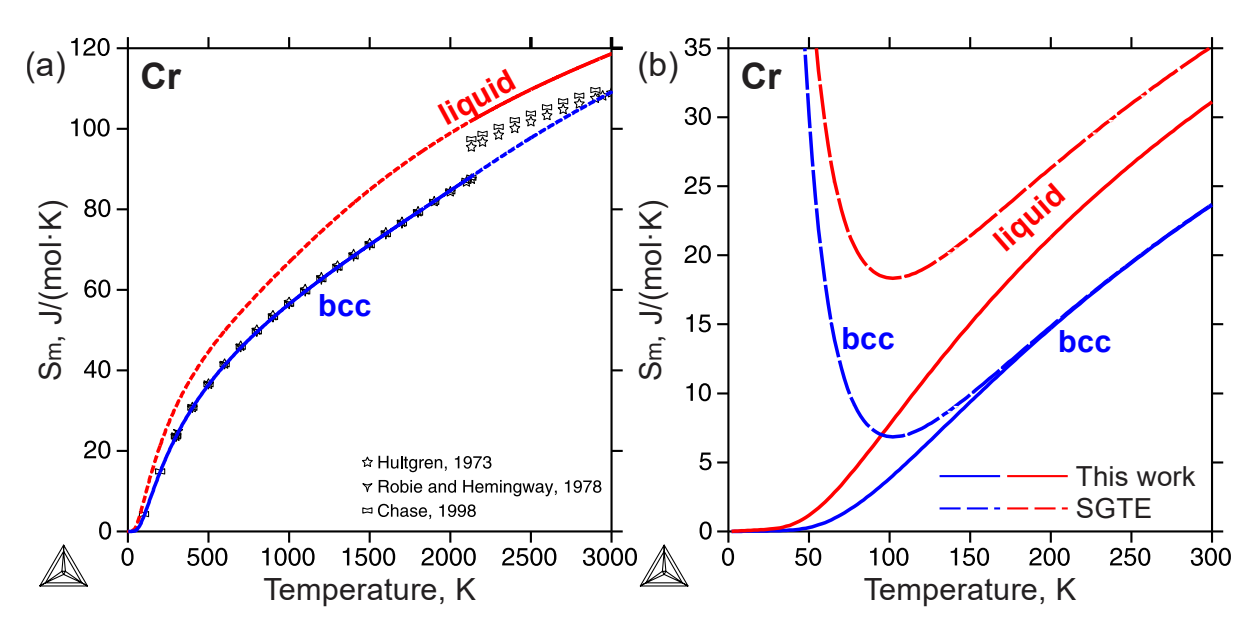


**Figure 5.** (a) Comparison between the calculated and evaluated [37–39] entropy for bcc and liquid Cr; (b) Comparison between the calculated low-temperature entropy for bcc and liquid Cr by this work and the SGTE database [9].

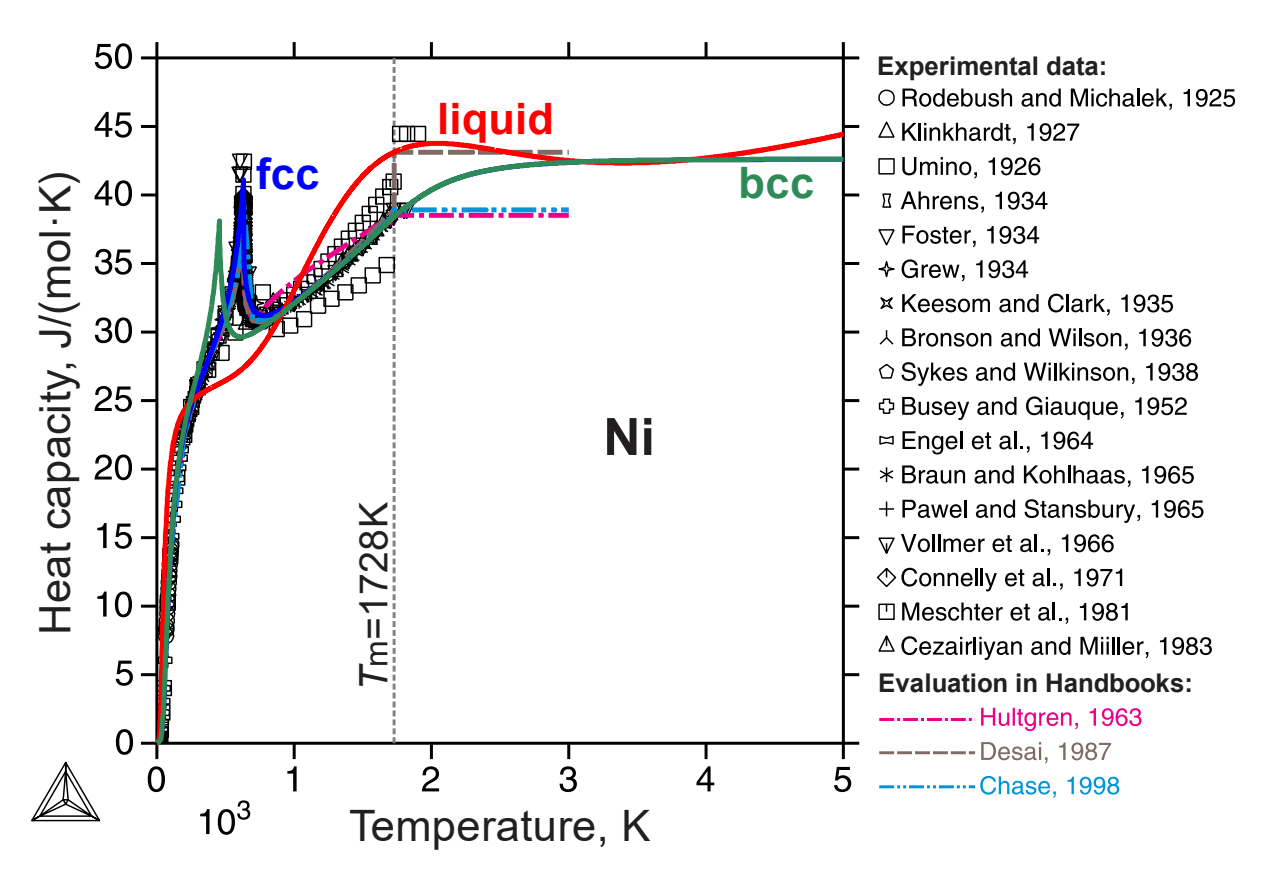


**Figure 6.** Comparison of the calculated heat capacities for fcc, liquid, and bcc Ni in this work with experimental datapoints [97,104,112,119,124–136] and evaluation by handbooks [36,39,113].

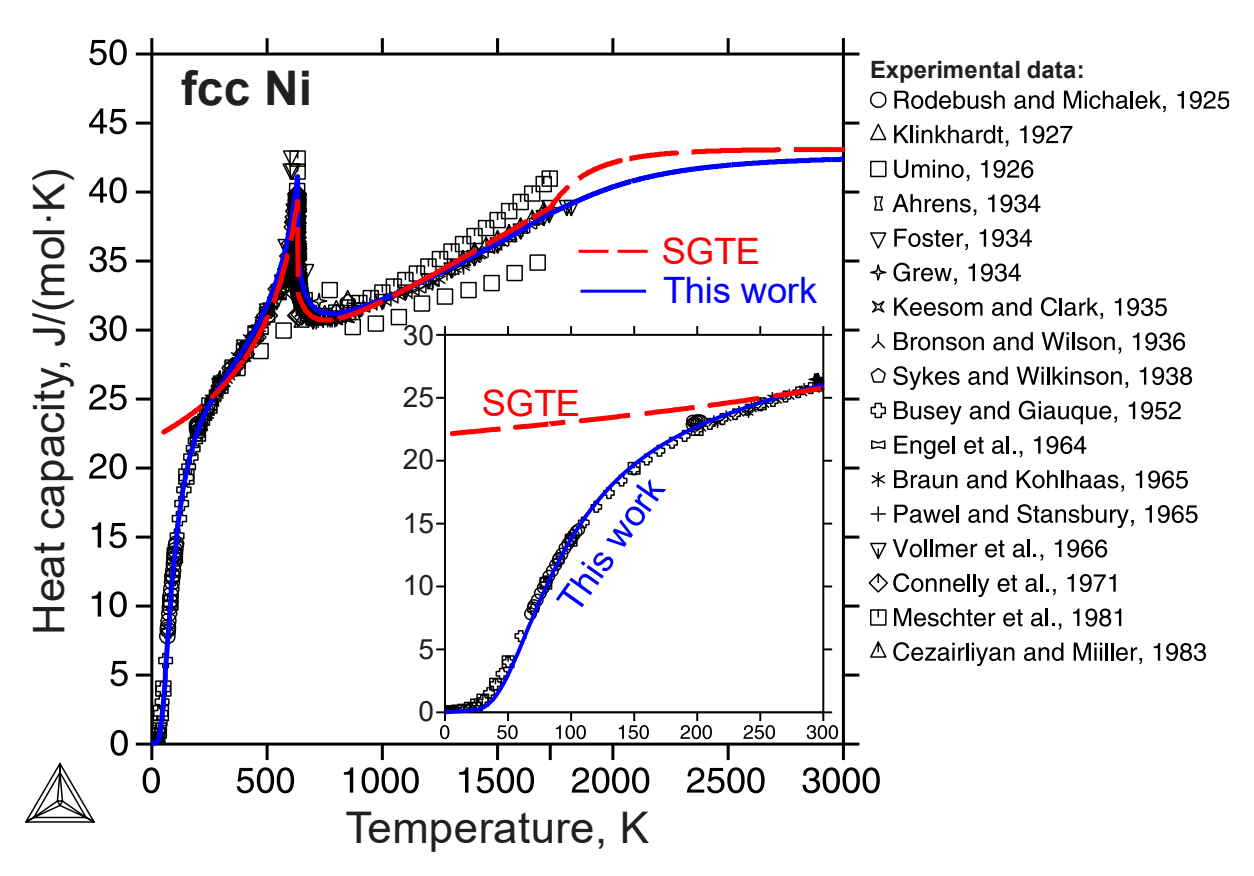


**Figure 7.** Comparison between the calculated heat capacity of fcc Ni in this work and by the SGTE database [9] with experimental results [97,104,112,119,124–136]. The low-temperature heat capacity from 0 to 300 K is magnified in the inset.

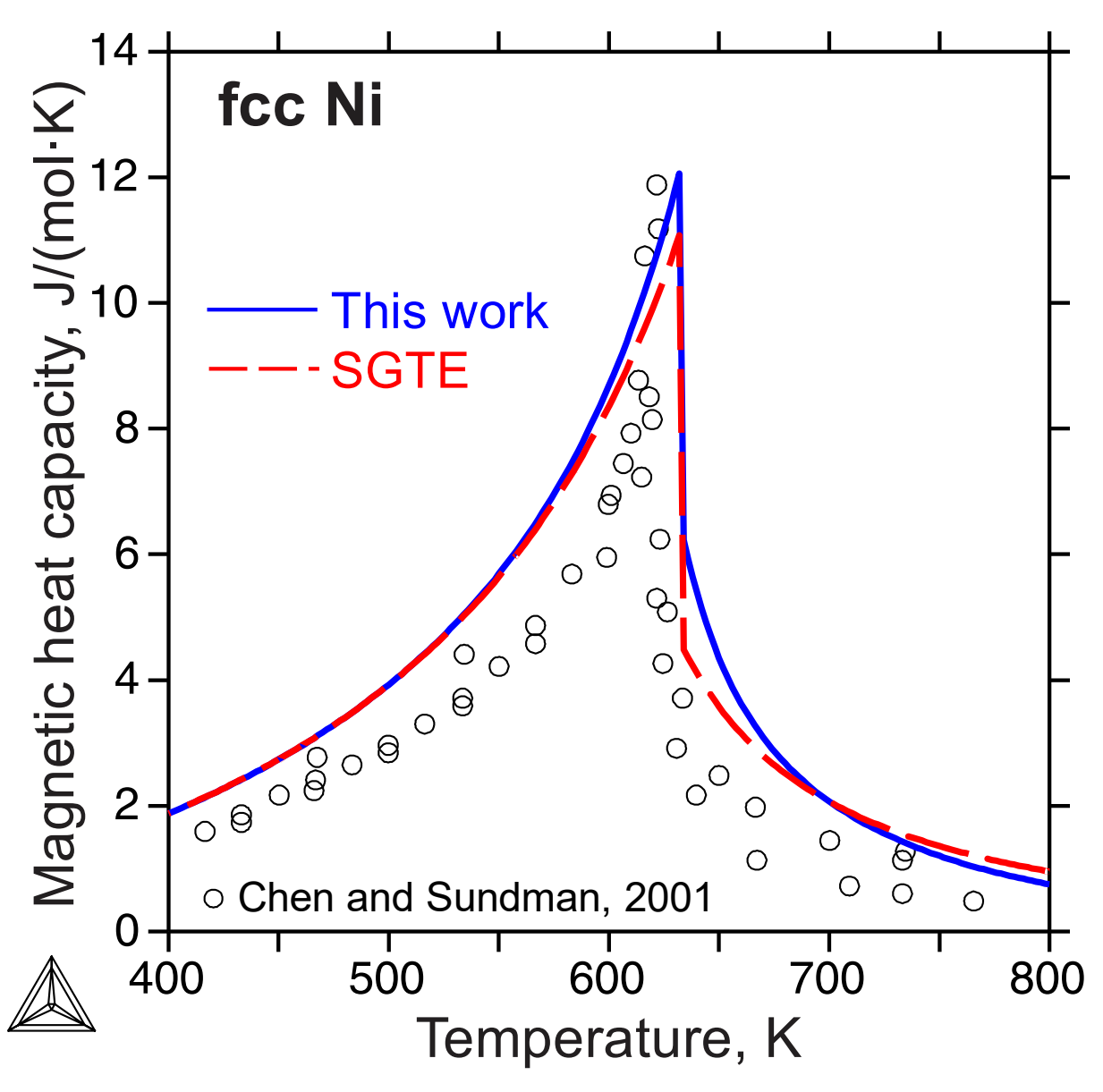


**Figure 8.** Comparison between the calculated magnetic heat capacity for fcc Ni using the IHX and IHJ models [9]. Datapoints are derived from experiments by Chen and Sundman [17].

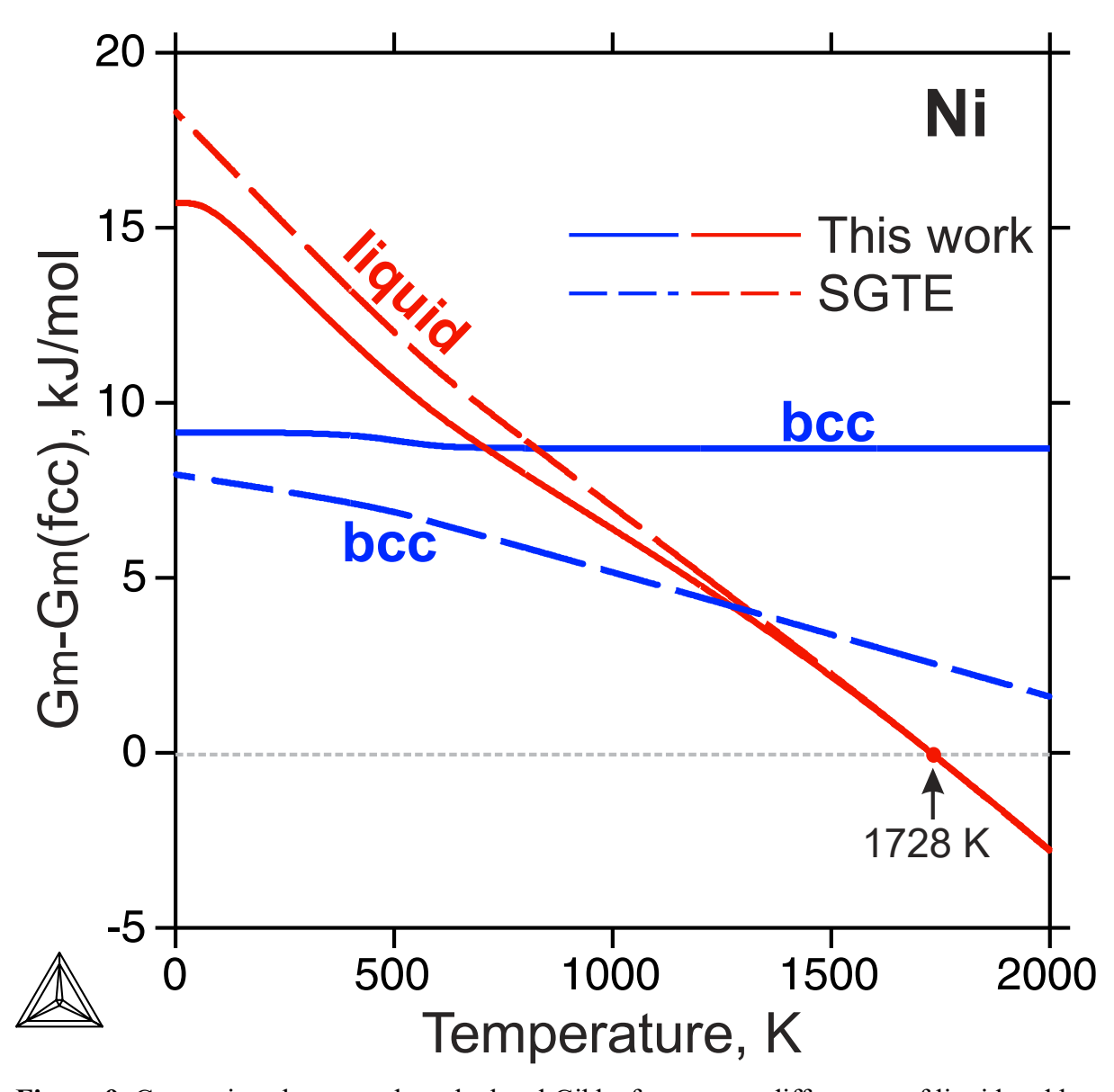


**Figure 9.** Comparison between the calculated Gibbs free energy differences of liquid and bcc Ni relative to fcc Nir in this work and by the SGTE database [9].

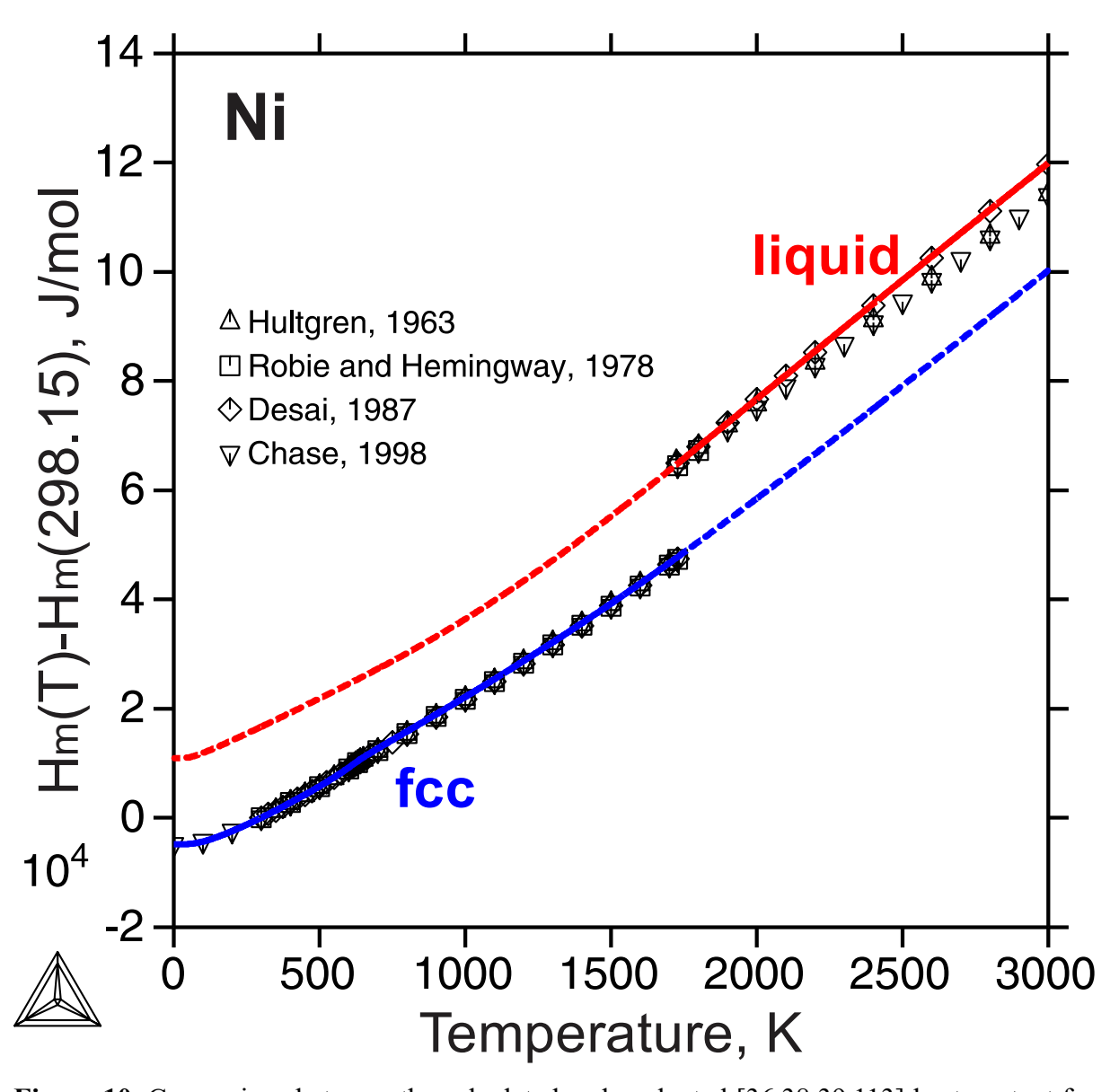


**Figure 10.** Comparison between the calculated and evaluated [36,38,39,113] heat content for fcc and liquid Ni.

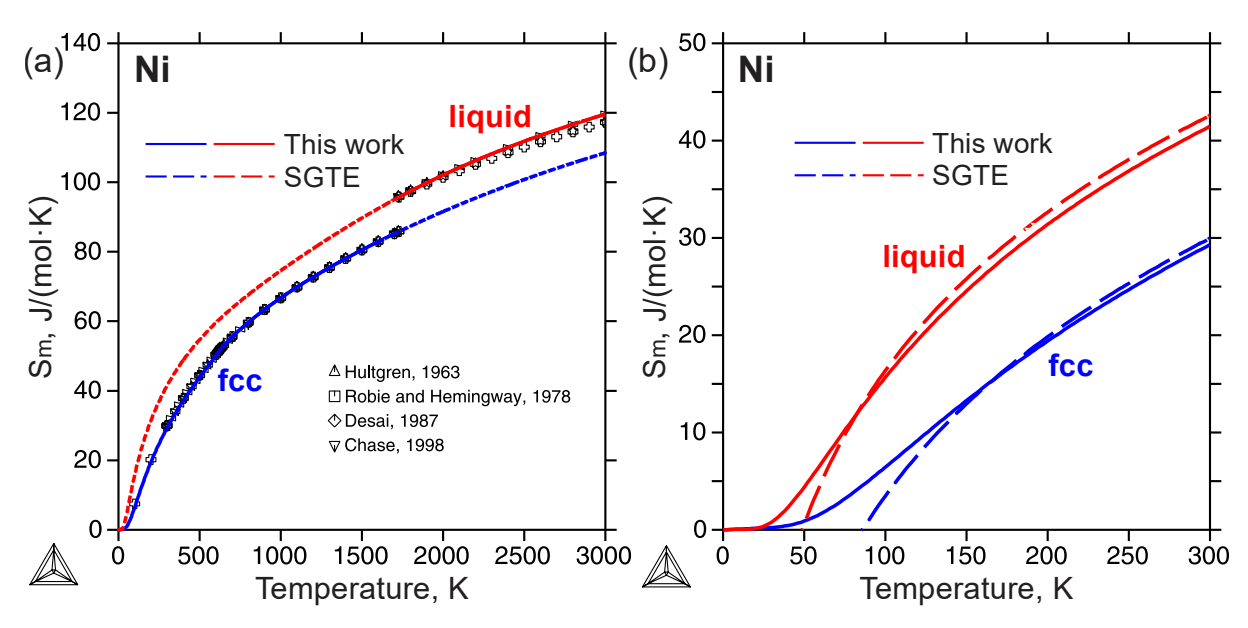


**Figure 11.** (a) Comparison between the calculated and evaluated [36,38,39,113] entropy for fcc and liquid Ni; (b) Comparison between the calculated low-temperature entropy for fcc and liquid Ni by this work and the SGTE database [9].

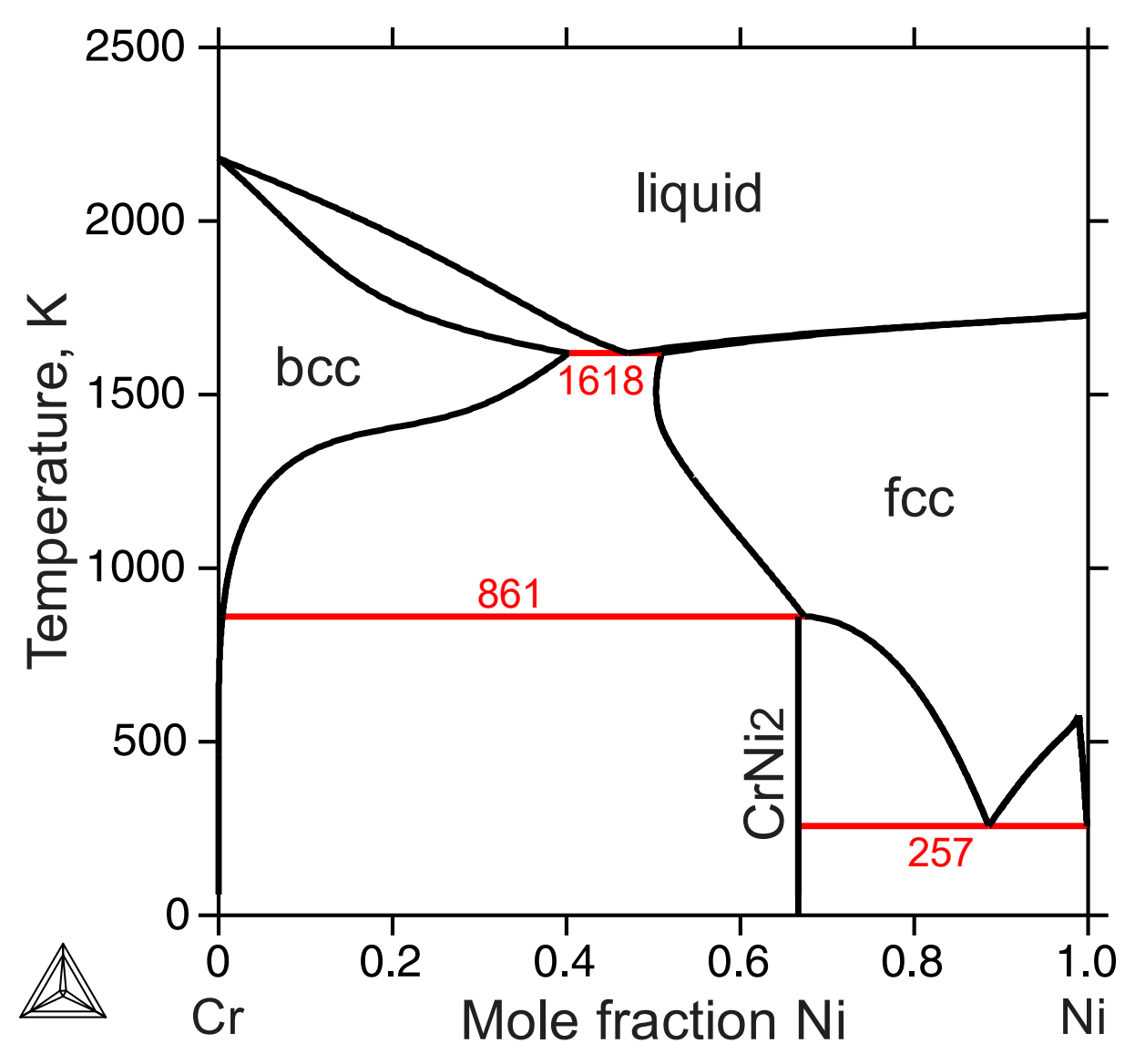


Figure 12. The calculated Cr-Ni phase diagram by Tang and Hallstedt [152].

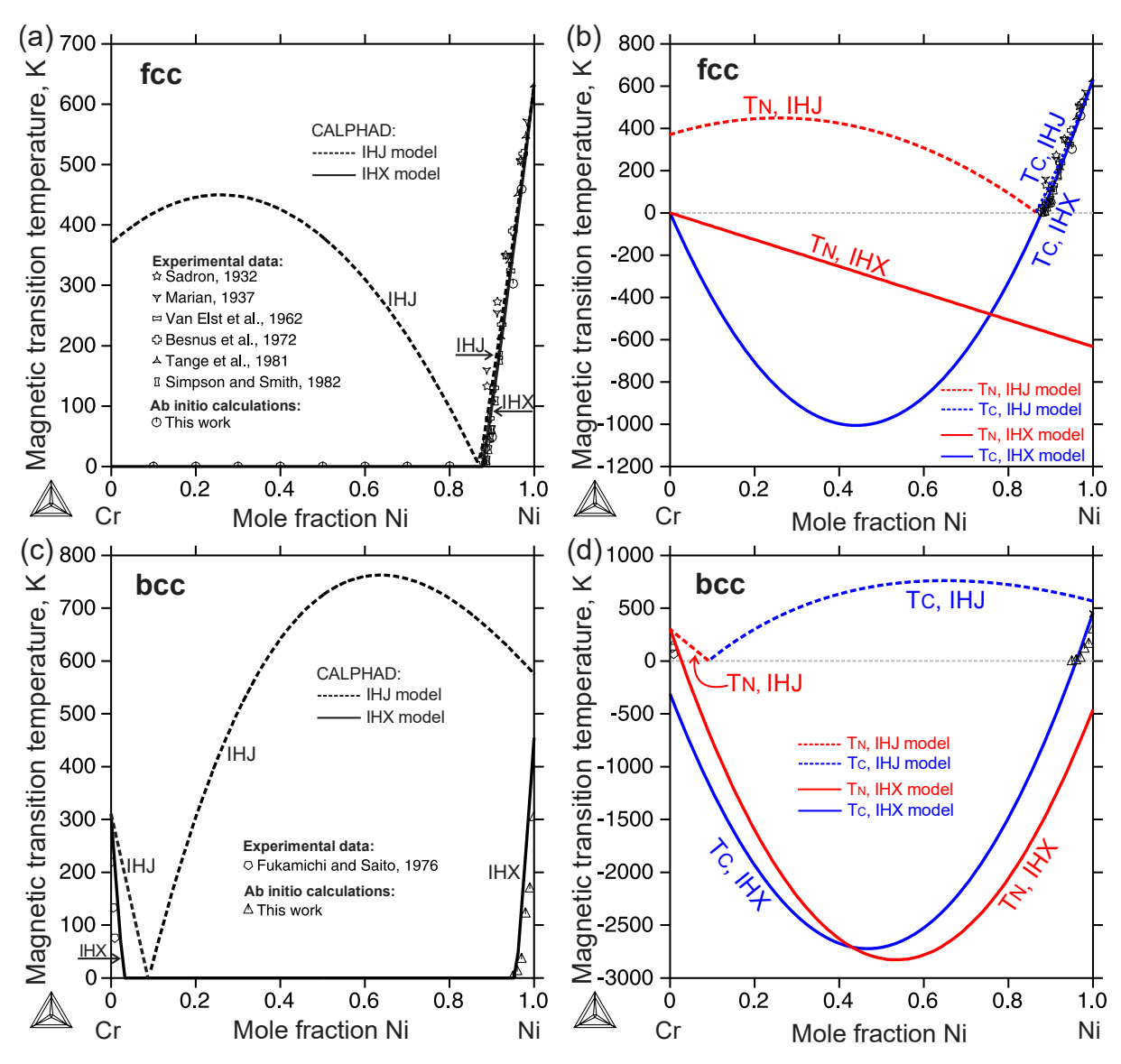
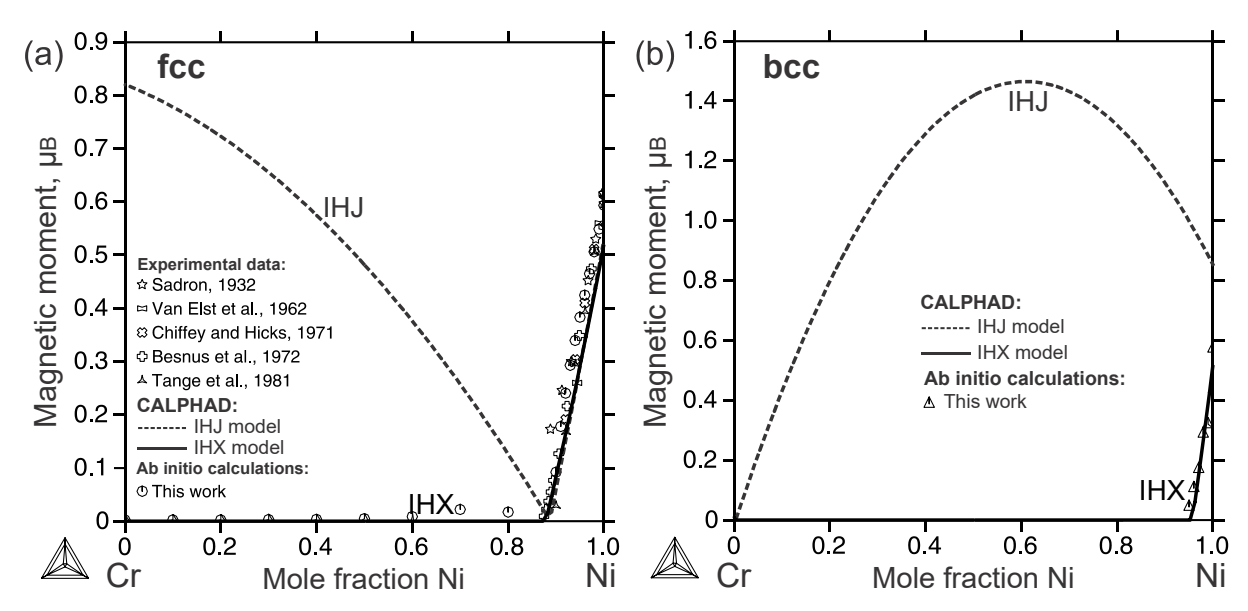
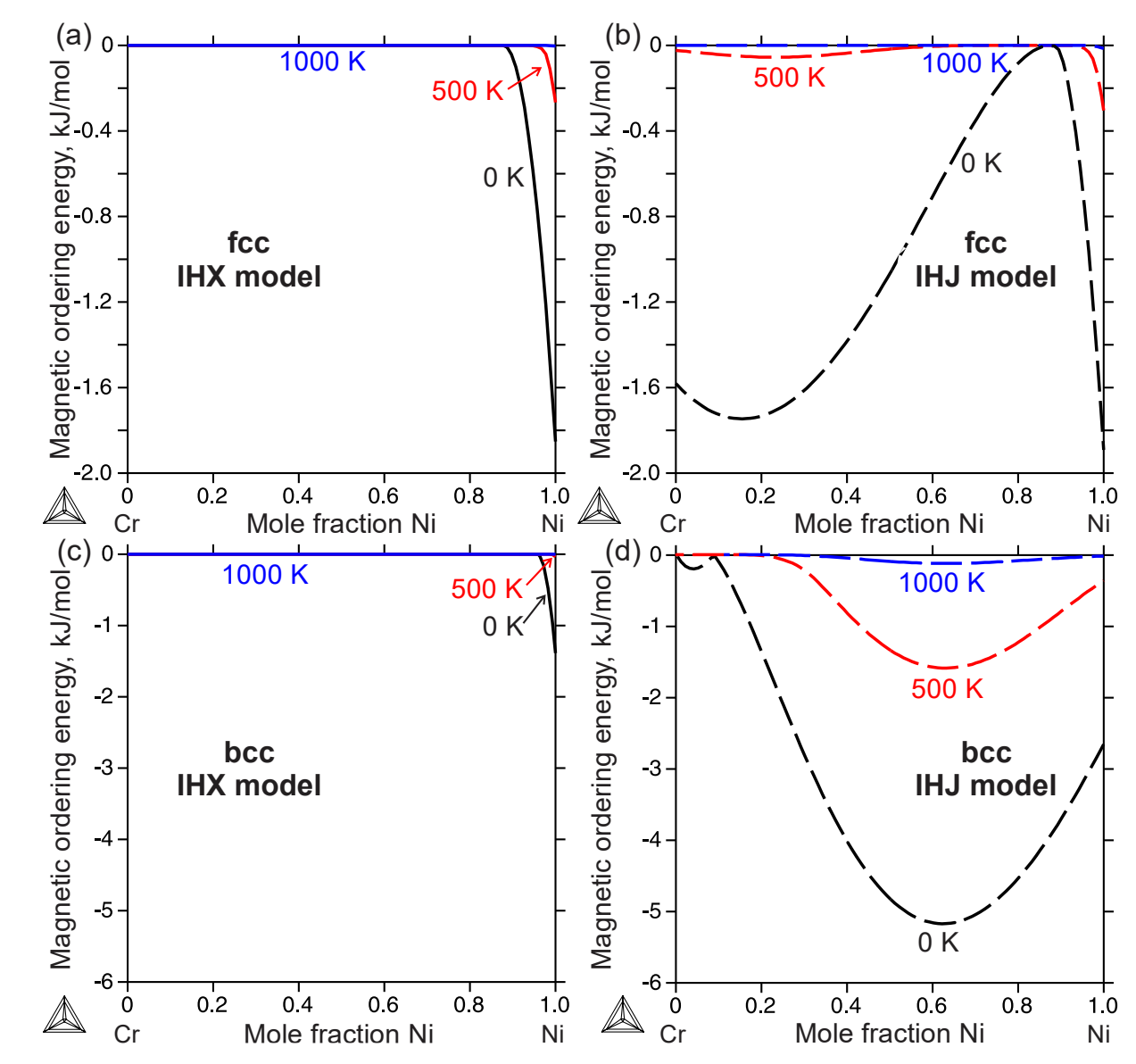


Figure 13. (a) Comparisons of the calculated magnetic transition temperature by the IHX and IHJ [148] models with experimental results [116,182–186] for the fcc Cr-Ni phase; (b) Demonstration of numerical treatment using both IHJ and IHX models for Curie and Néel temperatures of the fcc alloys; (c) Comparisons of the calculated magnetic transition temperature by the IHX and IHJ [148] models with experimental results [187] for the bcc Cr-Ni phase; (d) Demonstration of numerical treatment using both IHJ and IHX models for Curie and Néel temperatures of the bcc alloys.



**Figure 14.** Comparisons between the calculated magnetic moment in this work using the IHX model and by Lee [148] using the IHJ model for (a) the fcc; and (b) the bcc solution phases. Experimental magnetic moment data for the fcc phase are taken from [116,121,182,184,185].



**Figure 15.** Comparisons between the calculated magnetic ordering energy in this work using the IHX model and by Lee [148] using the IHJ model for (a)(b) the fcc phase; (c)(d) the bcc phase at 0, 500, and 1000 K.

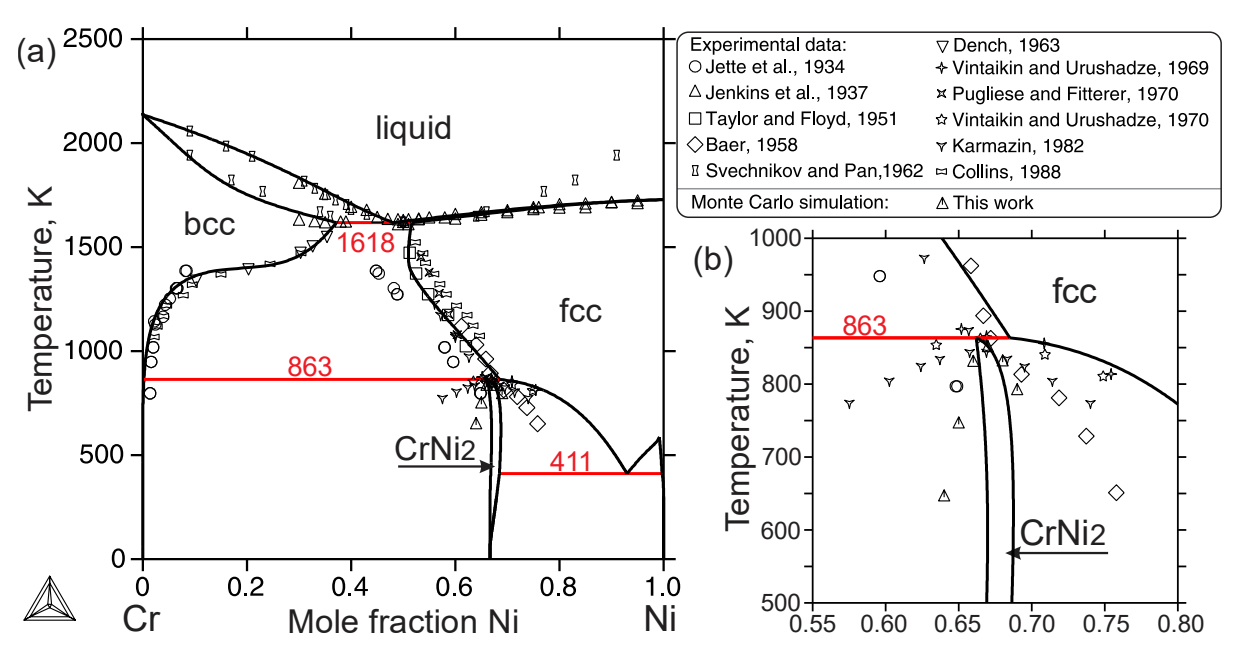


**Figure 16.** (a) Comparison between the calculated and experimental [158–168] Cr-Ni phase diagram; (b) Magnification of the CrNi<sub>2</sub> phase region.

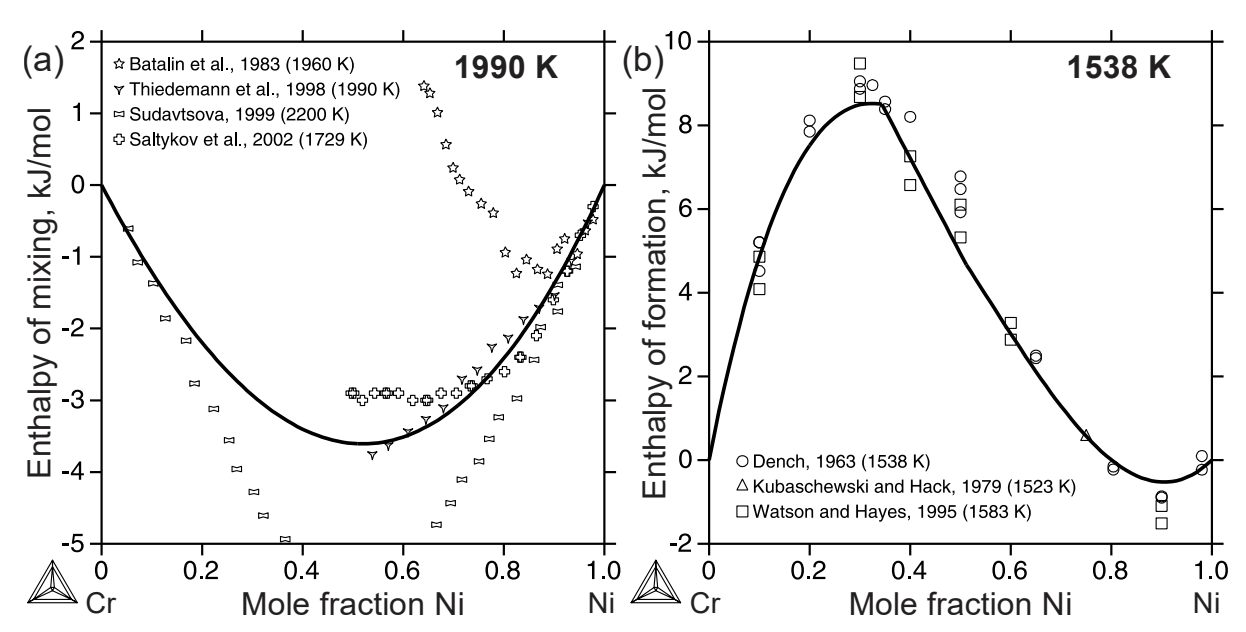


**Figure 17.** (a) Comparison between the calculated and experimental [153,154,169,170] enthalpy of mixing for the liquid phase at 1990 K. The reference state is liquid Cr and liquid Ni. (b) Comparison between the calculated and experimental [163,171,172] enthalpy of formation for the solid phases at 1538 K. The reference state is bcc Cr and fcc Ni.

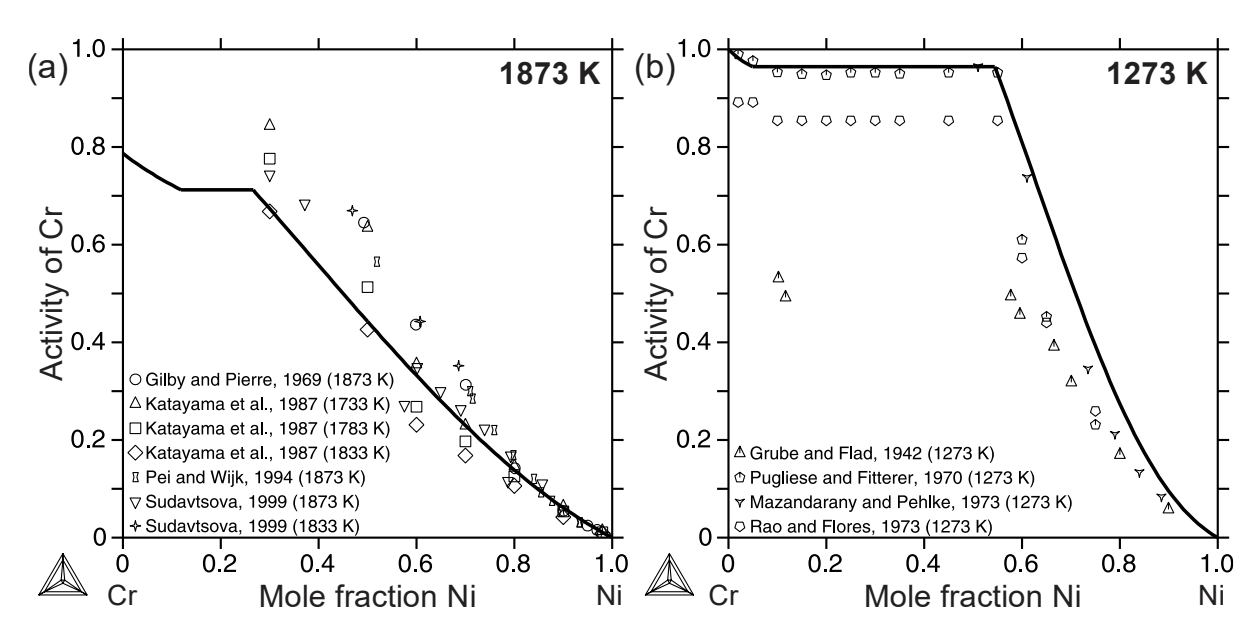


**Figure 18.** (a) Comparison between the calculated and experimental [170,173–175] activity of Cr at 1873 K, relative to liquid Cr; (b) Comparison between the calculated and experimental [168,176,179,180] activity of Cr at 1273 K, relative to bcc Cr.